ARTICLE

Journal of Micromechanics and Molecular Physics

Coarse-grained atomistic modeling of dislocations and generalized crystal plasticity

Alex Selimov*, Kevin Chu* & David L. McDowell*,†,‡

Abstract Recent developments in generalized continuum modeling methods ranging from coarse-grained atomistics to micromorphic theory offer potential to make more intimate physical contact with dislocation field problems framed at length scales on the order of microns. We explore a range of discrete dynamical and continuum mechanics approaches to crystal plasticity that are relevant to modeling behavior of populations of dislocations. Predictive atomistic and coarse-grained atomistic models are limited in terms of length and time scales that can be accessed; examples of the latter are discussed in terms of interactions of multiple dislocations in heterogeneous systems. Generalized continuum models alleviate restrictions to a significant extent in modeling larger scales of dislocation configurations and reactions, and are useful to consider effects of dislocation configuration on strength at characteristic length scales of sub-micron and above; these models require a combination of bottomup models and top-down experimental information to inform parameters and model form. The concurrent atomistic-continuum (CAC) method is extended to model complex multicomponent alloy systems using an average atom approach. Examples of CAC are presented, along with potential to assist in informing parameters of a recently developed micropolar crystal plasticity model based on a set of sub-micron dislocation field problems. Prospects for further developments are discussed.

Keywords Crystal plasticity; atomistics; coarse-graining; generalized continuum; micropolar.

1. Introduction

The notion of crystalline plasticity modeling pertains to dislocation phenomena manifesting at length scales from 0.1 nm to hundreds of micrometer, associated with the evolution of dislocations in crystals across a range of corresponding length scales, with time scales ranging from fs to years. In the spirit of the early influence of Professor A. Cemal Eringen aimed towards the concept of micromorphic media [1] and the historical development of generalized continuum (GC) methods (see e.g., Refs. 2–4, we will focus on model frameworks that express nonlocal spatial interactions as ultimately necessary to model the evolution of dislocation structures. Several key model constructs have been introduced that provide support for understanding based on simulations within selective subdomains of length and time scale. These include fully resolved atomistic modeling (e.g., molecular dynamics (MD)), coarse-grained atomistic approaches such as the quasicontinuum (QC) method [5–8] and concurrent atomistic-continuum (CAC) method [9–22], microscopic phase field (MPF) models [23–26], discrete dislocation dynamics (DDD) [27–31], statistical continuum dislocation (SCD) models [32–49], mesoscopic GC crystal plasticity models of slip gradient type [50–60], and less well developed and implemented micromorphic [61–64] and micropolar [65–70]. This work focuses on the recent advances in coarse-grained atomistics, specifically the CAC method, in modeling higher numbers of dislocations and dislocation–obstacle interactions than are accessible to conventional atomistics. Some examples of CAC are presented for various aspects of modeling dislocations in crystals. After outlining a recently developed micropolar crystal plasticity framework and drawing parallels to nonlocal slip gradient crystal plasticity, the paper closes with suggestions for overlapping bottom–up CAC and DDD simulations with micropolar crystal plasticity theory by solving submicron scale dislocation field problems to inform the parameters of GC crystal plasticity models, which are then applicable to much higher length and time scales.

2. Hierarchy of Defect Structure

Defect structures at various levels of spatial hierarchy control properties of crystalline materials. Dislocations serve as primary carriers of plastic deformation and assemble in non-equilibrium, metastable configurations that constitute dislocation substructure. Metal plasticity is fundamentally associated with processes of nucleation, generation, migration, interaction, trapping, and annihilation of dislocations in crystals and polycrystals [71–73]. This substructure plays a key role in higher length scale (e.g., polycrystalline) work hardening, for example. The number of accessible

*School of Materials Science and Engineering, Georgia Institute of Technology, Atlanta, GA 30332, USA
†Woodruff School of Mechanical Engineering, Georgia Institute of Technology, Atlanta, GA 30332, USA
‡david.mcdowell@me.gatech.edu
‡Corresponding author.

Received 1 September 2021; Accepted 10 February 2022; Published 6 April 2022; doi:10.1142/S2424913021420133

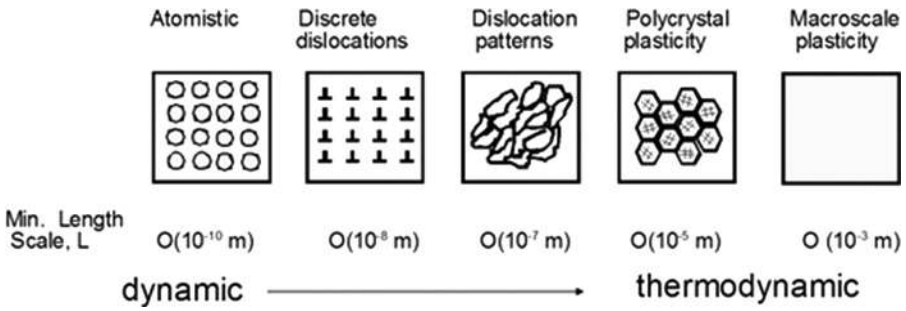

Fig. 1. Hierarchy of length scales in crystal plasticity ranging from atomic (resolution of dislocation cores), to configurations of dislocations, patterning at the mesoscale, and up to multiple grains/phases at the scale of structural applications. The primary length scale gap in modeling and simulation exists in describing the patterning of dislocations as necessary to bridge discrete simulations at left with continuous field representations at right [74].

dislocation configurations to accommodate deformation decreases as the length scales of structures (grains, multilayers, etc.) reduce to hundreds and then tens of nanometers, giving rise to increasingly important effects of slip gradients in material strengthening, with a strong influence of the slip system back stress. Figure 1 depicts five levels of structure hierarchy, ranging from the atomic structure of lattices and interfaces (atomistics) to migration and interaction of configurations of dislocation line segments (discrete dislocations), collective pattern formation of dislocations (dislocation substructure), heterogeneous plastic flow within sets of grains/phases (polycrystal plasticity), and finally up to the scale of engineering applications where underlying structure (dislocation structures, grains and phases) is "smeared" by considering an equivalent macroscopic set of properties or responses. The minimum length scale typical of each of these levels is also shown in Fig. 1, and ranges from interatomic spacing to mean free path for dislocations, to grain size, and up to characteristic dimensions of components or structures of interest.

Time scales of interest for processes at each level of structure hierarchy vary in the dynamic to thermodynamic transition indicated in moving from left to right in Fig. 1. Dynamic atomistic simulations typically range from picoseconds to nanoseconds, while large-scale discrete dislocation dynamics simulations can extend to the order of seconds. At far right in Fig. 1, polycrystal and macroscale plasticity models can address time scales relevant to that of large-scale laboratory specimens or structural applications, i.e., ranging from milliseconds to years depending on the applied strain rate.

Multiscale models of dislocation plasticity are necessary to simulate various properties/responses of interest over a wide range of length scales. Goals may differ according to the scales addressed. The interested reader may consult comprehensive recent in-depth review by McDowell [73]. Chemical reactions, lattice elasticity, and defect nucleation are typically governed by atomic scale structure and energies (defect, surface, etc.), while the elastic stiffness and yield point of polycrystals involve many grains and or phases. The rate of material strain hardening is closely related to dimensions and morphology of the dislocation substructure. Reduced order models are employed to address phenomena corresponding to scales to the right in Fig. 1 and reflect cooperative thermodynamics and kinetics of dislocations in crystals. On the other hand, discrete models that apply to scales at the left in Fig. 1 are of fully dynamic character or employ an overdamped dynamical scheme, tracking locations of individual atoms or defect segments. Degrees-of-freedom (DOF) necessary to characterize the structure of a fixed volume of material decrease from left to right in Fig. 1; in so doing, the information necessary to characterize the dynamical state is discarded in favor of achieving a reduced order continuum thermodynamic description. Stochastic response of ensembles of dislocations is recognized as a hallmark of these intermediate scales or "mesoscales," motivating the use of statistical methods to represent material behavior.

3. Overview: CAC Method

The CAC method is a spatial coarse-graining strategy for concurrent multiscale modeling that was developed as an application of atomistic field theory [9], with a local density function used to connect this continuum theory to atomistics via multiscale balance equations [10–13]. CAC employs a two-level structural description of crystalline materials [10] that is based on an extension of the lattice statistical mechanics approaches of Irving and Kirkwood [75, 76]. This leads to a concurrent atomistic-continuum representation of the conservation laws of mass, momentum, and energy [9, 77, 78]; the reader is referred to a series of papers for details [10, 13, 18, 22]. In particular, the paper by Xu *et al.* [18] provides details for addressing quasistatic coarse-grained simulations of dislocations in crystals, and the recent overview of Chen *et al.* [11, 12] is a comprehensive presentation of the mathematical and implementation bases for CAC. The dynamic implementation includes full inertial effects that can address phonon interactions with wavelengths above the element size, see e.g., Xiong *et al.* [17, 79, 80] and Pluchino *et al.* [81]. Governing equations are listed in the appendix that pertain to the implementations of CAC employed in this paper.

Since CAC employs a three-dimensional (3D) integral formulation of the governing field equations with a non-local force field, interelement continuity is not required; dislocations or cracks can therefore nucleate and propagate as an emergent behavior via sliding and separation between elements with or without adaptive coarse-graining [14–17]. CAC does not employ the Cauchy–Born assumption throughout the coarse-grain domain; dislocations can be modeled throughout the entire solution domain, whether at full atomistic resolution or coarse-grained. This sets it apart from fully concurrent methods that require full atomistic resolution at the dislocation core, such as QC. In contrast to the QC method, which has the objective of seeking convergence of the solution to that of the fully atomistic case for various field problems, CAC differs in its goals. Increasing the element size in CAC increases the coarse-graining error systematically by virtue of the process of interpolation of atomic positions; the benefit of this tradeoff is a reduction of degrees of freedom due to coarse-graining while still able to model propagation of dislocations. CAC can be used to obtain such

information locally in fully resolved regions of interest, while maintaining acceptable accuracy of the solution of the overall field problem to support quantitative insights and provide input to calibrate higher scale continuum mesoscale models; we shall give some examples later in this paper. Given inherent epistemic uncertainty in the interatomic potential(s), such coarse-graining error in mesoscale problems can be viewed as a systematic function of mesh density, still serving the purpose of predictive bottom−up simulations of many body defect interactions. For example, CAC can coarse-grain atomistics in regions away from certain domains of interest and still capture long-range fields and interaction stress fields of dislocations, while preserving high accuracy in fully resolved atomistic regions of interest. If trends of behavior or collective mechanisms are to be considered as a function of microstructure or stress state, as is often the case in DDD, then CAC may offer a more predictive pathway to support such parametric studies to inform DDD. Coarse-graining error in CAC can be minimized via adaptive remeshing [20], based on the level of the relative nodal displacement between elements; in fact, this is necessary for general field problems to allow dislocation migration along arbitrary extended slip planes. Such remeshing, if desired, need not conform to full atomistic resolution, but can involve simply splitting larger elements into smaller ones, still containing many atoms per element.

In many other approaches based on domain decomposition or coarse-graining, so-called "ghost" forces arise from a change of the underlying continuum formulation and energy summation rules; these issues do not arise in CAC because the underlying integral formulation and constitutive framework (i.e., the interatomic potential) are invariant with respect to coarse-graining. CAC has parallels to peridynamics [82], an integral form nonlocal particle-based model that adopts more of a mesoscale strategy rather than building on the underlying interatomic potential of the atomistic system, see e.g., Sun and Sundararaghavan [83] for a GC smeared treatment of dislocations in crystal plasticity.

Elements in CAC can contain a varying number of atoms defined by unit cell multiples, with element boundaries corresponding to close-packed planes (i.e., slip planes). For FCC crystals, rhombohedral isoparametric elements have been employed in which element surfaces correspond to octahedral slip planes with the two outer surface layers (2NN elements) of atoms within each element subject to different interpolation functions than those used in the element interior, providing the ability to accommodate stacking faults corresponding to partial dislocation migration between elements. The generalized stacking fault energy curve of full atomistics can be accurately reproduced even for nearly 10,000 atoms per element [18], including both the stable and unstable stacking fault energies. More layers of surface elements can be introduced to accommodate more spatially extended atomic rearrangements associated with continued twinning partials or other topological (surface related) phase transformations, if necessary. CAC implementations for HCP or BCC crystals characterized by dislocations with more complex core spreading or dissociation require further advances in terms of element types that admit these dissociation modes, if necessary. Otherwise, these processes can always be captured by modeling at full atomic resolution, while providing approximation in coarse-grained regions. The number of atoms per element can differ within the mesh of a given field problem; CAC field solutions can consist of fully atomistic domains adjacent to coarse-grained domains with tens to thousands of atoms per element. Dislocations can move between fully resolved atomistic regions and coarse-grained domains along interelement boundaries rather seamlessly [14, 18], preserving the essential nature of partial dislocations.

An obvious application of CAC, as also the case for the QC method, is the simulation of dislocation pile-ups at interfaces and progression of slip transfer reactions as multiple dislocations sequentially react at the interface (i.e., processes involving transmission, reflection, absorption and desorption). This is a technologically very important problem related to the contribution of interface reactions on work hardening. The same is true for dislocation−obstacle interactions, whether a given obstacle is encountered by successive dislocations or a set of dislocations encounter an array (periodic or random) of obstacles. This class of problems is extremely computationally challenging using fully resolved atomistics at length scales large enough to capture dislocation pile-ups; periodic unit cell simulations with full atomistics sacrifice reality of randomness and engender potentially high image forces. Furthermore, if exercised as finite temperature molecular dynamics, the desired dislocation interactions will be overdriven (far from equilibrium) and characteristic of shock plasticity rather than the thermally assisted flow regime. To make contact with experimental measurements, realistic boundary conditions (e.g., free surfaces) are often necessary; transmission electron microscopy (TEM) thin foil observations of dislocation reactions offer one example. Some noteworthy features of CAC implementation are listed in the following:

(i) The CAC implementation employs weak form 3D continuum finite element approaches. The interatomic potential is the only constitutive relation, as in fully resolved atomistics. There is no need for an artificial interface between the full atomistic and coarse-grained atomistic domains.

(ii) Dynamic CAC [13–17, 79, 80, 84, 85] is equivalent to MD for fully atomistic resolution and can simulate complex crystalline materials and reproduce both acoustic and optical branches of phonon dynamics due to its incorporation of internal degrees of freedom. It is useful for coarse-graining of full dynamics, including polyatomic (multicomponent) materials, for a given lattice structure. It can be used with or without an ensemble thermostat, and there are special considerations for treatment of the coarse-grained contributions to the microkinetic energy. It can also be employed for finite temperature dislocation mobility studies, for example, including multicomponent alloys where an average atom formulation is used in the coarse-grained region [86]. The finite-temperature quasicontinuum hot-QC method [87, 88] and coarse-grained molecular dynamics (CGMD) methods [89, 90] have facilitated coarse-grained multiscale MD simulations at finite temperature based on a local harmonic approximation to estimate entropic effects of the atoms not explicitly represented in the model. Finite temperature methods for CAC are in early stages in terms of modeling dislocation field evolution. Elevated finite temperature simulations for quasistatic (near equilibrium) and non-equilibrium dynamic conditions, as well as heat transport via modes other than phonons remain to be fully developed for CAC. Most finite temperature dynamic CAC applications to date have not considered a thermostat (we will demonstrate one such application for finite temperature dislocation mobility later in this paper). Detailed consideration based on statistical mechanics of coarse-grained kinetic energy at finite temperature have been recently advanced by Chen *et al.* [11, 12], and this is an active research area.

(iii) Quasistatic CAC [18–21, 91–94] is a variant in which the dynamic CAC implementation at very low homologous

temperature is constrained by quenched dynamics at each time step, with conjugate gradient or FIRE energy minimization [94] performed periodically (e.g., every 50 time steps) to ensure that the system is not overdriven by high rates [18, 19, 73]. Therefore, it can faithfully represent reaction pathways of dislocations characteristic of quasistatic, thermally assisted deformation conditions, in spite of the use of ~fs time steps. In other words, the solution accords with the concept of a sequence of constrained equilibrium states in internal state variable theory for nonequilibrium defect evolution [95, 96]. Accessible solution times are still constrained by the time step required in the fully atomistic regions, as the Velocity Verlet technique is used to march forward in time [18].

(iv) In view of (ii) and (iii), CAC provides speedup relative to full atomistics by virtue of spatial coarse-graining for time-marching problems, up the order of 1–2 orders of magnitude depending on the problem.

(v) For true static problems (0 K), energy minimization using CAC with coarse-graining away from domains with atomic structure of interest can substantially reduce computational effort required for energy minimization. This can facilitate, for example, application of the nudged elastic band (NEB) method [97, 98] to compute activation energy of extended defect interactions with obstacles.

Some limitations of current implementations of CAC can also be noted, many of these already mentioned. First, there are different ways to address coarse-grained finite temperature implementation of the governing equations and the microkinetic energy is particularly challenging in this regard [11, 12]. Second, limitation of element boundaries to close-packed planes restricts available dislocation pathways and abrupt changes in element size may artificially impede dislocations since they move along interelement boundaries; these issues can be dealt with by adaptive mesh refinement and development of new elements with more complete rendering of slip systems. These limitations are being addressed in an ongoing work. Dislocation cross-slip cannot be modeled accurately, nor twin growth/thickening, in coarse-grained regions; thus, in regions near interfaces or obstacles where it is important to accurately model cross-slip, refined meshes or full atomistic models are required. Finally, while CAC has been employed to study multiple dislocation pile-ups, for example, it is not intended as a replacement of DDD, which studies collective behavior of large dislocation networks and ensembles.

Of course, CAC and QC are not the only atomistic coarse-graining methods. For example, the early works of Rudd and Broughton [89, 90] and generalized particle dynamics (GPD) applied to atomistic systems [99] have been introduced, although not applied in the context of dislocations in crystals. GPD would require remapping to full atomistic resolution to address dislocations, analogous to QC.

4. Examples of CAC Applications for Dislocation Plasticity in Crystals

The quasistatic implementation of the CAC method [18] is relevant to modeling dislocation plasticity in that it approximates thermally assisted dislocation reaction pathways. Use of quenched dynamics with periodic energy minimization enhances efficiency for problems with defects by reducing the load on periodic energy minimization. The quasi-static implementation is considered useful for modeling physically representative reaction pathways in the potential energy landscape for thermally assisted dislocation processes since it is not overdriven, as typical of MD simulations. Applications to date of the quasi-static implementation have been limited to monoatomic systems, while multicomponent systems have been considered in dynamic CAC applications.

4.1. Dislocation pile-ups at interfaces

A logical application of CAC is the simulation of dislocation pile-ups at interfaces in extended domains and progression of slip transfer reactions as multiple dislocations sequentially encounter an interface (transmission, reflection, absorption and desorption). Of interest is whether remnant dislocation debris from prior reactions modify each successive incoming dislocation reaction, an obvious basis for work hardening. Without predictive atomistic simulations, intuitive assertion of mechanisms such as continued build-up of Orowan loops can dramatically overpredict work hardening in certain cases and foster incorrect attribution of unit processes. The efficiency of quasi-static CAC simulations has been exploited by Xu *et al.* [92] to simulate dislocation pile-ups with leading screw character against both (a) a $\Sigma3$ coherent twin boundary (CTB) and (b) a $\Sigma11$ STGB in Ni [92], with the interface represented with a thin "ribbon" of material on each side at full atomistic resolution and coarse-grained elements elsewhere. The size of the simulation domain approaches that of TEM foil dimensions reported in the literature, with traction-free boundary conditions applied on the top and bottom surfaces to realistically model dislocation migration and reactions from experiments as well as the influence of the free surface on modifying dislocation flux. In such simulations, coarse-grained elements with thousands of atoms per element are employed everywhere in the simulation domain (>100 nm spatial dimension) except for a narrow (5−10 nm) fully atomistic region along the interface. As an example, Fig. 2 shows successive encounters of dislocations impinging on a $\Sigma3\{111\}$ CTB in Ni. Owing to the improved efficiency of such large-scale simulations (by 1−2 orders of magnitude relative to full atomistic simulation), CAC facilitates parametric studies of the predictive capabilities of multiple alternative embedded atom method (EAM) interatomic potentials to model successive pile-up dislocation interactions with $\Sigma3$ interfaces in Ni for thin foil specimens [92], thereby supporting sensitivity studies to assist in judging the quality of these empirical potentials. These CAC simulations for Ni were compared to full MD simulations and high-resolution TEM experiments in Xu *et al.* [92].

4.2. Sequential interactions of dislocations with obstacles

Another recent application of quasi-static CAC by Xu *et al.* [93] considers sequential interactions of five incoming dislocations in a pile-up with fields of obstacles in pure FCC Al to better understand sequence effects of reaction debris on successive dislocation reactions, with obvious implications for work hardening.

Figure 3 shows the computational set-up for an array of edge dislocations impinging on an obstacle with diameter of several nm. This study explicitly compares the dislocation−obstacle interactions in distinct cases of an impenetrable precipitate and a void. A uniform linear array of obstacles along the incoming dislocation line is introduced via periodicity in the x-direction. When the obstacle is a void, all dislocations sequentially shear the void into two hemispheres until the void becomes fully split into two separate pieces which pose less significant barriers to subsequent dislocation motion. This bypass mechanism implies that the barrier strength of a void is dominated by its interaction with the first dislocation in the

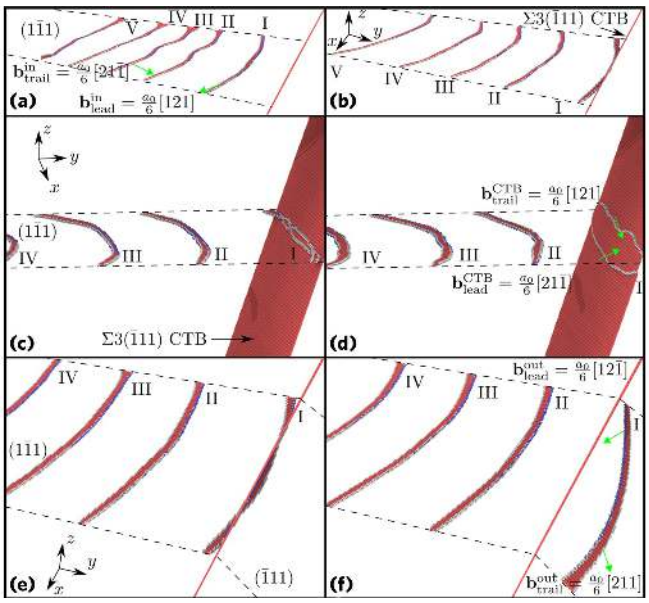

Fig. 2. Snapshots in time of a pile-up of a/2[110] dislocations with dominant leading screw character successively impinging on a Σ3{111} CTB in Ni, (b) showing constriction of leading and trailing partial dislocations. Atoms are colored by adaptive common neighbor analysis; red corresponds to HCP local crystal structure, blue are not coordinated as either FCC or HCP, and all FCC atoms are deleted. In (c) and (d), three of the EAM potentials considered in this parametric study predict incorporation of the dislocation into the interface, with two partial dislocations gliding on the twin plan in opposite directions. In (e)−(f), the other two EAM potentials considered predict that the dislocation cross-slips into the outgoing twinned grain via redissociation into two partials. This same kind of study of various empirical potentials for extended quasi-static field problems can be valuable to support selection of a specific EAM potential, or as an exercise supporting improved machine learning potentials [92].

array and by its size. When the obstacle is an impenetrable precipitate centered on the glide plane, an alternating process of Orowan and Hirsch looping mechanism occurs from one incoming dislocation to the next. The first, third, and fifth dislocations leave behind a shear loop around the precipitate, while the second and fourth dislocations transform the newly formed Orowan loop into two prismatic loops, bypassing the precipitate following the Hirsch looping mechanism. This sequence suggests that after the bypass by a series of successive dislocations, obstructive debris does not accumulate around the precipitate, unlike the classical understanding inferred by a single dislocation/precipitate interaction. Contrary to prior studies, defects are not created in the dislocations that glide away from the obstacle. These results suggest reconsideration of conventional thought regarding the roles of voids and precipitates in strain hardening and hysteresis behavior under cyclic loading.

4.3. Dislocation pile-up interactions with semi-coherent phase boundaries

The interactions between lattice dislocation pile-ups and semi-coherent phase boundaries are also of interest as they lead to emergent properties observed in material systems such as nanolaminates. Selimov *et al.* [94] used CAC to study the effects of stress fields induced by such dislocation pile-ups, generated via nanoindentation on the misfit dislocation structure of both Ni/Cu and Cu/Ag semi-coherent {111} interfaces. Critically, as opposed to the many full atomistic studies that can be found in the literature [100−104], model geometries employed here included large interface segments, facilitated by CAC coarse-graining, to allow for non-homogenous evolution of the misfit dislocation structures. These investigated interface segments had dimensions of approximately 80 × 40 nm, containing many interface misfit dislocation junctions. Atomistic model geometries with smaller interface segments, often containing only a single misfit dislocation junction, generally employ periodic boundary conditions that impose artificial symmetry on the interface structure evolution. This can lead to unrealistic predictions for slip transmission resistance as the local misfit dislocation density along the lattice dislocation impingement site has been shown to affect slip transmission [105, 106]. Here, slip transmission refers to the absorption of a dislocation into the interface and then nucleation/emission of a different dislocation into the neighboring layer, generally along the nearest parallel slip plane. These processes are coupled such that the absorption of the dislocation directly provides the energy and excess Burgers vector content for nucleation and emission into the neighboring layer. Work by Selimov *et al.* [94] found that the stability of the interface misfit structure depends on the misfit dislocation spacing. The investigated Ni/Cu interface, which has a larger misfit dislocation spacing than the Cu/Ag system, showed large distortion of the interface misfit structure, including localized expansion/compression of the misfit spacing as shown in Fig. 4. This asymmetric evolution of the dislocation structure is less significant for the Cu/Ag interface. As a result of this misfit pattern distortion, the slip transmission resistance of the Ni/Cu interface is expected to decrease due to the reduced local misfit dislocation density as a result of the motion of misfit dislocation junctions away from lattice dislocation impingement sites. This is expected to be an important consideration for accurately capturing the evolution of dislocation structures in multilayered materials. Future studies which directly link the slip transmission resistance of the interface to the misfit dislocation density can be used to calibrate reduced order models for these material systems.

Studies by Xu *et al.* [107] on Si/Ge (111) semi-coherent interfaces using CAC show the effects of misfit dislocation spacing on the slip transmission resistance of the interface. The CAC models investigated here reduced the degrees of freedom from 1.13 billion in the equivalent full atomistic model to 39.96 million atoms and nodes in the CAC model. The three primary ($\bar{1}11$) interface geometries were generated with different experimentally observed misfit dislocation structures but with the same atomic elements and crystal structure in each phase. As a result, the slip transmission resistance of the various interface types can be attributed primarily to the differences in the misfit dislocation structure. Slip transmission is related to the peak local stress on the lattice dislocation slip plane as shown in Fig. 5(d). This shear stress is calculated for atoms near the interface but is resolved to the incoming lattice dislocation slip plane and glide direction using a new flux formulation for atomic stress [108]. Applied stress drives the lattice dislocation towards the interface until absorption. Continued loading causes the stress on the interface to increase until the nucleation and emission of a dislocation into the neighboring layer. This causes a relaxation of the interface stress. Higher values of peak local stress imply higher activation energies required to nucleate a dislocation after absorption. Thus, this metric can be used as a measure for slip transmission resistance. The interface with the largest resistance to slip transmission had the highest density of interface misfit dislocations. It was also found that slip transmission required the absorption of multiple dislocations into the interface, highlighting the importance of cooperative

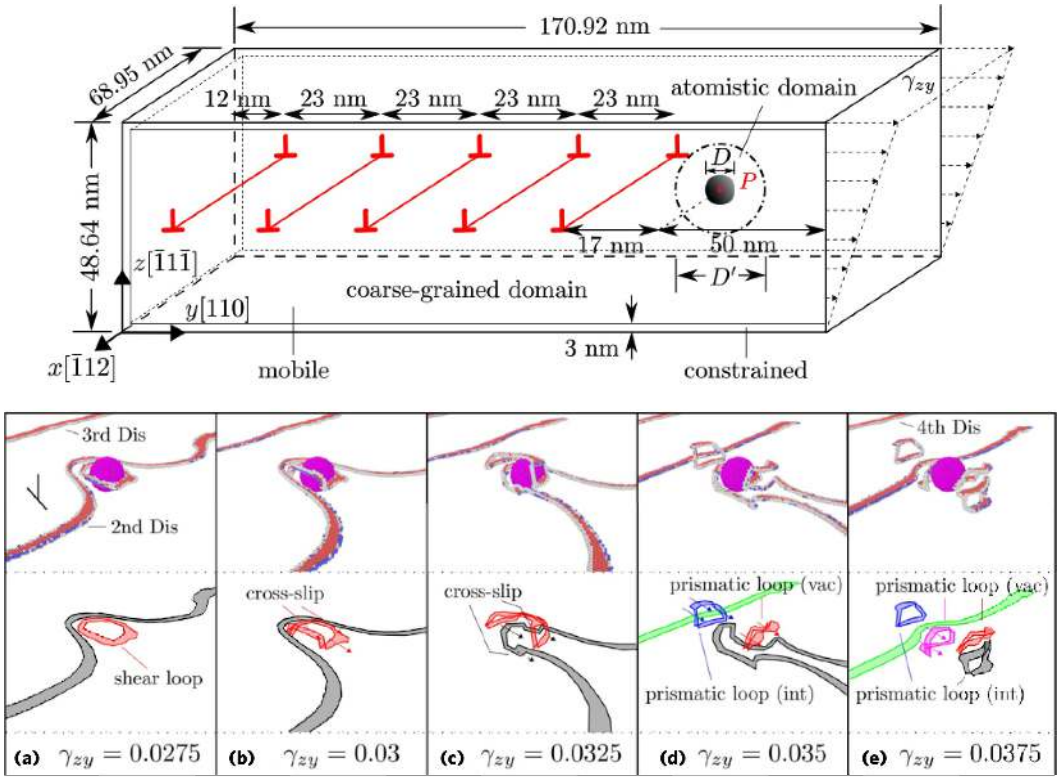

Fig. 3. Illustration (top) of the simulation cell for interactions between five edge dislocations in a planar array and an obstacle (filled black sphere centered at the red point P with diameter D), which is either a void or an impenetrable precipitate in distinct simulations [93]. An atomistic domain is meshed within a sphere centered at P with diameter D′ to let the obstacle deform and dislocations evolve at full atomic resolution, while the coarse-grained domain with 3D rhombohedral finite elements is employed elsewhere. Five initially equally spaced edge dislocations in the coarse-grained domain having the same Burgers vector a/2<110> are placed on the same [111] slip plane. Snapshots (bottom sequence) of the second edge dislocation bypassing an impenetrable precipitate with $D = 5:6$ nm following the Hirsch looping mechanism. In the first row, atoms on the precipitate surface are rendered in magenta. In the second row, different dislocations are distinguished by colors [93].

dislocation interactions (Figs. 5(a)−5(c)). Reaction pathways observed in this work can be used to directly inform allowed dislocation reactions in DDD models of such material systems. The rank ordering of interfaces based on slip resistance can furthermore be used as validation for reduced-order models to ensure that model forms faithfully reproduce structure/property relations. Study of the effects of dislocation debris deposited at the interface as a result of partial slip transmission on subsequent reactions is also important for the development and calibration of slip-dependent interface strength evolution terms. These sequential interaction studies are largely inaccessible to fully resolved atomistic methods due to the length scales required.

Additional comparisons between CAC simulations and reduced order models can be achieved via computation in a small neighborhood of relevant continuum quantities from the discrete simulations. Formulations presented by Tucker *et al.* [109] and Zimmerman *et al.* [110] have previously been used to compute continuum metrics, such as deformation gradient, atomic strain, and microrotation, which is of relevance to GC theories. Extension of these formulations to the coarse-grained finite element regions in CAC should be straightforward. It is also possible to compute dislocation density on the fly for various slip planes that coincide with interelement discontinuities from the finite element nodal positions. Total dislocation density can be computed using the relative position of FE nodes, and the geometrically necessary dislocation (GND) density can be computed based on the net Burgers vector over a selected Burgers circuit (e.g., given number of elements). These calculations would be much faster than dislocation density calculations based on fully atomistic models, such as the dislocation extraction algorithm (DXA) [111]. This speedup in the coarse-grained models results both from the reduced number of finite element nodes compared to the fully resolved atomic positions, and the richness of information contained in the magnitude of inter-element discontinuities along slip planes. These topics are being pursued in an ongoing work.

4.4. Average-atom method for multicomponent systems

The recent development of mean-field or average-atom (A-atom) EAM interatomic potentials to homogenize multicomponent systems at varying compositions has presented a promising avenue for representing bulk alloy properties in CG CAC regions. Average elastic constants, lattice parameters, and the full generalized stacking fault energy curve are matched closely by the A-atom representation [112]. For alloys in which solute strengthening is the primary mechanism, it is important to capture locally varying strain fluctuations associated with true random solute types. Screw dislocation mobility calculations [113] shown in Fig. 6 confirm that the locally varying strain fields associated with heterogeneous solutes in the lattice are critical in describing dislocation glide behavior and thus yield strength. Fully A-atom simulations resemble that of pure metals and show negligible Peierls stress, further illustrating the

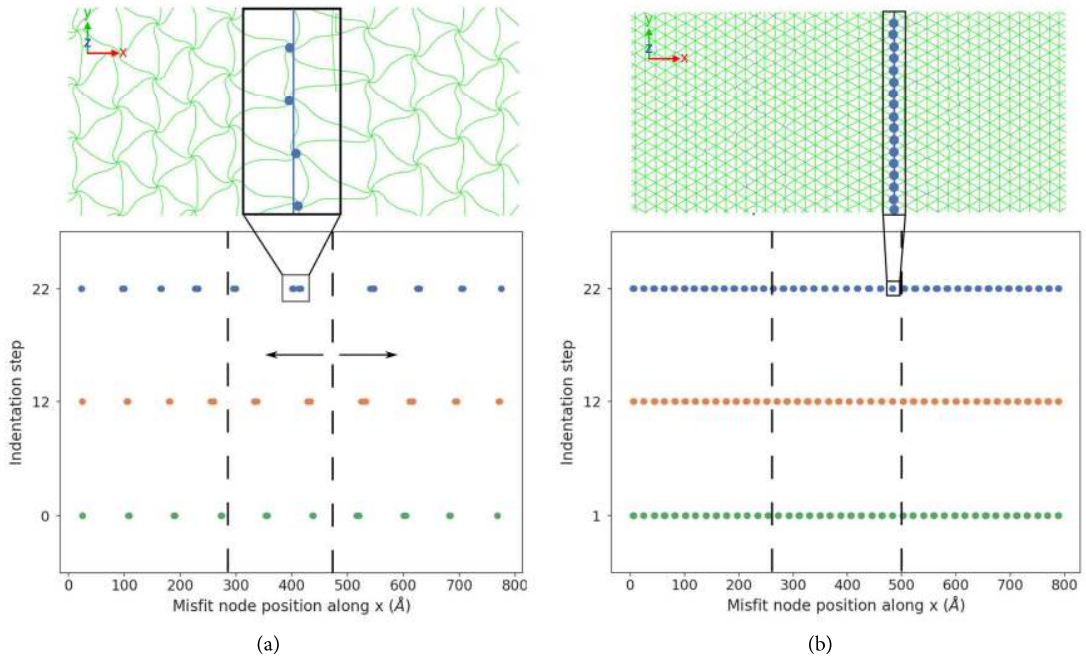

Fig. 4. Position of misfit dislocation junctions along the x-direction for three different indentation steps for (a) Ni/Cu and (b) Cu/Ag. Dashed lines represent the impingement positions of incoming lattice dislocations generated via nano-indentation. Larger number of indentation steps are associated with increased proximity of lattice dislocations to the interface and higher magnitudes of induced stress on the interface plane. Incoming lattice dislocation stress fields cause deformation to the interface misfit patterns for (a) Ni/Cu, as characterized by the movement of misfit dislocation junctions away from the lattice dislocation impingement position. Arrows indicate the direction of misfit dislocation junction motion. Predictions of slip transmission resistance based solely on the misfit dislocation density of an ideal interface may overshoot actual values [94].

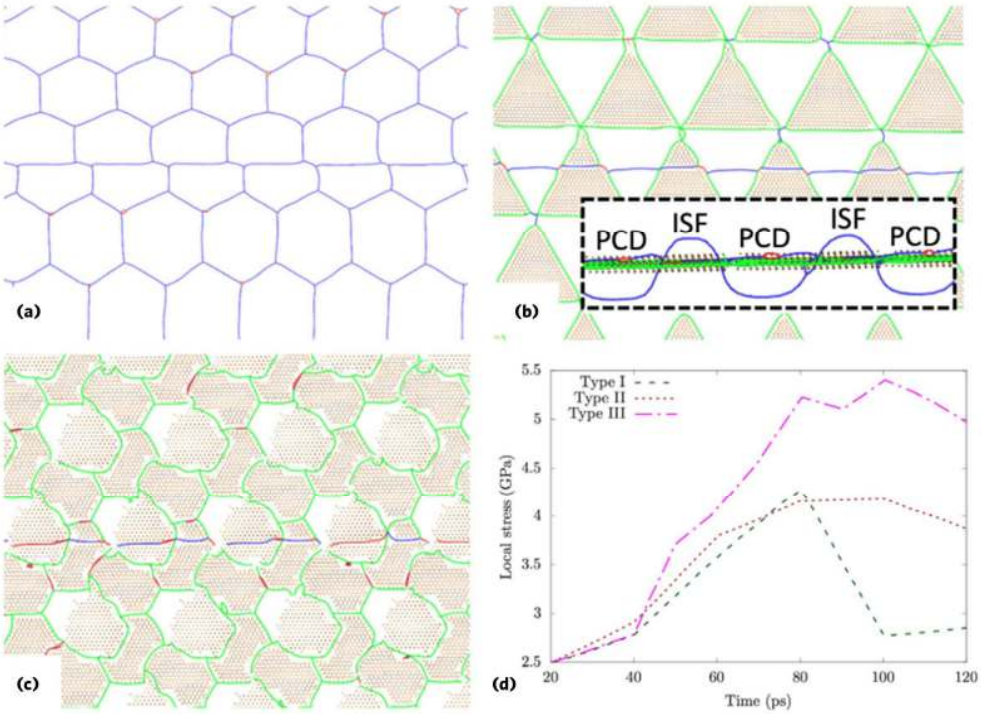

Fig. 5. (a)–(c) Atomistic configurations for three different types of Si/Ge semi-coherent interfaces upon their interactions with the first lattice dislocation originated from Si. ISF: intrinsic stacking fault; PCD: pristine cubic diamond. (d) The local stress for atoms near the interface is plotted with respect to time for all three types of interfaces. This local stress is the resolved shear stress which drives the lattice dislocation calculated using a new flux formulation for atomic stress [108]. Peak values relate to the resistance of the interface to slip transmission. The time starts at 20 ps, immediately following the dynamic relaxation and corresponding to the moment at which shear strain is applied to drive the dislocation motion [107].

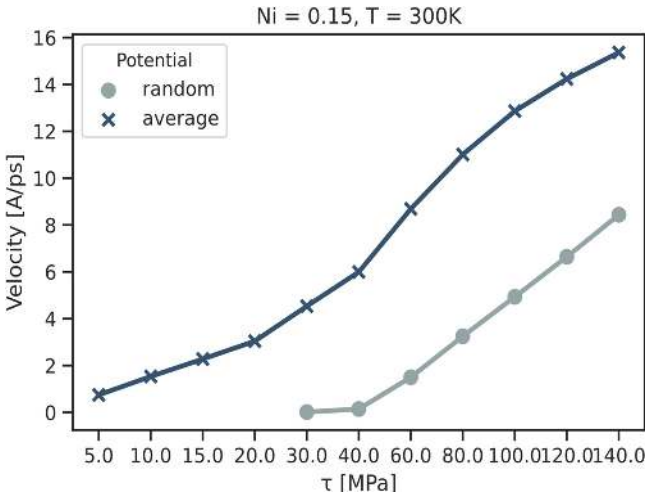

Fig. 6. Dislocation mobility curve comparison computed at full atomistic resolution using full random and A-atom representation at a fixed composition of $Fe_{70}Ni_{15}Cr_{15}$ at $T = 300$ K [113].

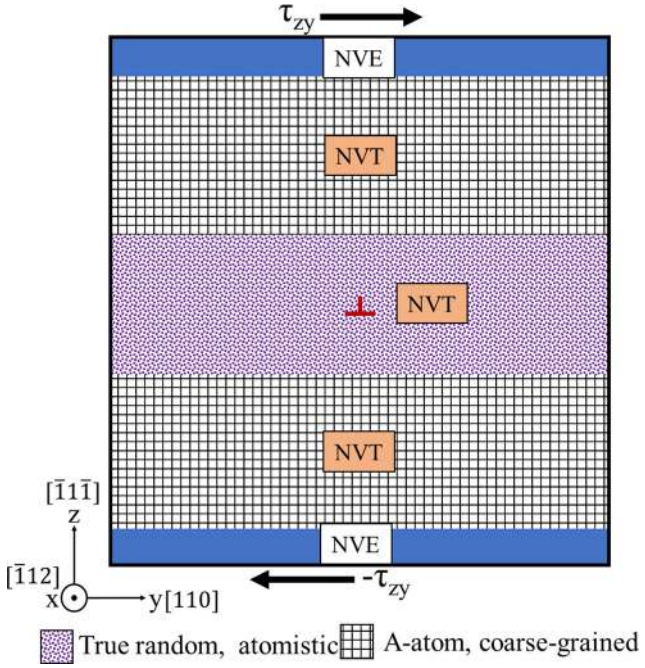

Fig. 7. Mobility model domain decomposition and ensemble definitions. Solid blue region denotes free surface boundary conditions. For simulations of this character, a ∼5 nm true random atomistic region is typically employed in the z-dimension [86].

importance of true solute representations. This finding is also consistent with simulations executed in polycrystalline alloy systems [114] and other medium entropy alloys [115]. Thus, fully resolved true random atom types or hybrid potentials in which A-atom interactions with true solutes are fully defined should instead be applied for simulations probing dislocation mechanisms in solid solution strengthened alloys.

In light of these observations, CAC simulations were executed with true multicomponent random solute types and fully resolved atomistics in a region of interest such as the dislocation glide plane and core. Away from the critical glide region, coarse-grained CAC elements are defined using full A-atom types, as shown schematically in Fig. 7. Employing such a chemical and spatial coarse graining strategy further decreases the computational cost associated with energy minimization away from the region of interest due to the smoothness of the potential energy surface and improves convergence. This is particularly relevant for EAM potentials that define systems with more than three constituent elements, such as with medium and high entropy alloys [116]. Molecular statics energy minimization of the mixed-resolution, mixed-representation model indicates that there are no spurious stresses associated with the transition from coarse-grained to atomistic representation and simultaneously A-atom to true random atoms. This is a significant improvement over calculations using other domain-decomposition approaches such as CADD [117] where spurious long-range stresses manifest at the interface between continuum and atomistic length-scales. Furthermore, there is no discontinuity in the stress fields computed in CAC from the true random dislocation core region to the A-atom CG region. This makes the combined CAC/A-atom approach a logical application to extended defect length scale simulations and longer-range stress field interactions due to reduced computational cost.

4.5. Dislocation mobility

Dislocation mobility laws are very important in DDD simulations, and A-atom CAC enables the efficient parametric study of fundamental dislocation behavior in compositionally complex alloy systems as a bottom−up approach. Edge dislocation mobilities are calculated in the FCC FeNiCr ternary system using the Zhou EAM potential to validate this approach [86]. A-atom/true random hybrid potentials are derived at three different compositions within the 3*XX* range of austenitic stainless steels. Simple velocity-rescaling approaches [118] are used to control temperature and implement a constant volume, constant temperature (NVT) ensemble. Mobility curves showing distinctive solute/phonon drag regions are derived, and the composition-dependent trends as predicted from solute-strengthening theory are quantified and closely match the results from full atomistics. These initial results support the use of A-atom in future CAC simulations of not only compositionally complex alloys, but any multicomponent system for which an empirical EAM potential exists. The application of CAC to extended defect length scales and heterogeneously distributed obstacle arrays as relevant to precipitate-strengthened multicomponent alloys is an obvious further extension of this approach.

Flow rules that describe thermally activated processes such as the bypass of individual point defects or chemical short-range order are employed by crystal plasticity finite element methods to approximate the underlying microstructural rearrangement at the mesoscale. In such approaches, the temperature-dependent flow rule captures the rate of evolution of dislocation-mediated slip based on the Kocks−Argon−Ashby form [119, 120], analogous to an Arrhenius activation process. Similarly, DDD methods may incorporate fixed values describing the evolution of dislocation network structure through cross-slip and bypass [121, 122]. The key parameter in such inputs is the activation energy barrier, describing the strain evolution as a function of the applied stress and current temperature. A number of methods such as the simplified improved string method [123] the control box method [124], and the NEB [125] have been developed to quantify the activation energy barrier. Among these, the NEB method has been most popular due to its

ease of use and general accessibility (available in public open-source packages such as LAMMPS [126]. The NEB method calculates a minimum energy path (MEP) between configurational states in two local energy minima describing the initial and final state of a unit process, separated by a saddle point. Displacement continuity and distance between intermediate "images" along the MEP are enforced through interconnected spring forces that realize a physically accurate picture of intermediate configurations along the reaction pathway. Improvements in algorithmic implementation such as climbing image [102] and free-end [127] variants improve NEB convergence for processes involving complex transition pathways, allowing for more precise determination of the saddle point energy. A transition state with high curvature requires a high density of images near the saddle point to resolve accurately. This is particularly relevant for stress-assisted, thermally activated processes such as those of dislocation bypass in FCC metals [128]. Accordingly, the computational cost of NEB remains high, as each image along the MEP is effectively an entire independent simulation system that must undergo constrained energy-minimized (with respect to the nudging and spring forces).

Such calculations are not limited to atomistic simulations, in fact the NEB procedure can be directly applied in other reduced order model forms such as DDD [129] to describe MEP trends at reduced cost. This requires that the model describes the self and interaction energies as a function of the dominant kinetic DOF for evolving attributes of microstructure and a continuous representation of the reaction pathway. CAC satisfies these requirements and is thus a suitable candidate for NEB simulations, particularly attractive for compositionally complex alloys since DOF are reduced significantly by coarse graining away from regions of interest, e.g., the dislocation core position and glide planes near critical obstacle bypass reactions. Simultaneously, the use of A-atom representation in such regions leads to improved convergence and decreased risk of becoming trapped in local energy minima [116]. Thus, CAC-NEB is a promising avenue for further length-scale bridging to mesoscale modeling techniques. The benchmarking of the combined coarse-grained NEB and A-atom representation for simple dislocation bypass reactions is a necessary precursor to applications involving more complex problems addressed using crystal plasticity.

CAC can be regarded as a continuum method that bridges between atomistics and DDD since it can address mesoscale dislocation configurations and long-range stress fields, along with detailed positions of individual dislocation lines. However, unlike DDD it models partial dislocations naturally and does not require prescribed rules for dislocation interactions/reactions with other dislocations, obstacles, or interfaces. Though not emphasized here, CAC can be used directly to inform nonlocal DDD approaches for core effects, as well as rules/heuristics for interface reactions and obstacle bypass.

5. Sub-Micron Scale Field Problems: Overlap of Bottom–Up Models with GC Models

While the label "crystal plasticity" has typically referred to the classical local continuum framework outlined by Asaro [130, 131] that assumes a continuously distributed population of dislocations moving on close-packed slip systems within a crystalline lattice, a more general perspective is warranted to address the spectrum of scales shown in Fig. 1. Atomistics and CG atomistic methods focus on the scales to the left in Fig. 1, while DDD models focus more on the mid-left up through dislocation substructures. GC models attempt to describe key effects of dislocation configuration in terms of low order attributes of substructure and extend upward to length scales to the right in Fig. 1; as such, they are useful for addressing initial-boundary value problems of dislocation plasticity in engineering.

It is instructive to consider what kind of overlap may reasonably be expected between length and time scale regimes between GC crystal plasticity models from top−down and bottom−up methods such as CG atomistics and more mesoscopic DDD. We desire to exploit such overlap to inform GC model parameter calibration by comparison to bottom−up methods. Bottom−up simulations have a large number of degrees of freedom to represent individual atoms (atomistics), collection of atoms (CG-atomistics), dislocations as distinct phase fields (microscopic phase field MPF models [23−25, 132] at atomic scale resolution, or discrete dislocation lines (DDD). In bottom−up atomistic or MPF models, dislocations emerge as lattice defects from atomic scale lattice rearrangement, either resolved at lattice spacing or via smeared gradient phase representations. Fully emergent dislocation processes (e.g., nucleation/generation) and interactions (long-range as well as short-range rearrangement reactions) can be modeled.

We consider DDD [27−31] to be appropriately described as a class of mesoscopic bottom−up model in which dislocation lines are introduced as objects embedded within a linear elastic continuum manifold. They are subject to prescribed source, interaction and cross-slip algorithms, propagate and interact, requiring assignment of mobility relations, junction strengths, and kinetics of thermally activated processes. As distinguished from bottom−up CG atomistic models that can reach to atomic scale and extend to moderate but limited mesoscales, they are not predictive in terms of atomic scale reactions. For example, CAC can model dislocation sources, unit processes of dislocation reactions with other dislocation and obstacles, junctions, and dislocation mobilities in a predictive, bottom−up manner to inform DDD. In DDD, Green's functions are employed to superimpose the stress fields associated with long-range dislocation interactions with the applied stress to compute the driving force on each segment, subject to overdamped conditions in a constitutive force−segment velocity relationship. Non-singular, non-local dislocation core effects on short-range dislocation interactions have been included [133] which improves the description of short-range interactions. The DDD method has received significant investment and is therefore maturing in terms of codes that support mesoscopic simulations, e.g., ParaDiS code [134, 135], and the microMegas code described by Devincre *et al.* [136]. Such codes can be used to study dislocation substructure formation processes that were heretofore inaccessible, see e.g., Ref. 137.

SCD models offer reduced order continuum descriptions compared to DDD by formulating the governing equations in terms of a statistical representation of the population/distribution of dislocations [32−49]. These models are more general in addressing statistical descriptions of dislocation densities than reduced order GC models and provide understanding similar to that gained from DDD.

All of these bottom−up methods are computationally intensive and largely unsuitable for large domains and/or long times necessary to support engineering analysis of structures or even polycrystalline or extended multiphase microstructures, etc. On the other hand, we can consider top−down, reduced order mesoscopic GC crystal plasticity models for this purpose. Early non-local or micromorphic GC models of elasticity and plasticity were not framed explicitly in the context of crystal plasticity and trace back half a century [138−141]. Advances towards addressing plasticity of crystalline

materials and dislocation patterning progressed after 1980 [142−144]. In the 1990s, as a first-order approach, GC crystal plasticity models adopted the lattice curvature induced by GNDs as the key to enrichment to capture size effects. Early models of strain gradient type [145−148] embedded the effects of strain gradients into scalar strength terms. In more recent works, slip system back stress was linked directly to slip gradients in crystal plasticity and manifests specimen configuration, loading configuration, size and boundary effects. Second gradient (plastic strain gradient or slip gradient) crystal plasticity models regularize the influence of strain gradients on the material work hardening behavior [50−60]. These models are applicable to micron length scale problems such as nano-indentation, torsion and bending of small specimens, and particle strengthening of dislocations. Being reduced order models, they can also be applied to much higher length scales, e.g., microstructure involving multiple grains/phases, although they are considerably more computationally intensive than standard local crystal plasticity models. Such models involve tracking slip system shears or shearing rates as additional variables to facilitate numerical estimation of slip gradients related to GND densities.

GC crystal plasticity models of strain gradient, micropolar and micromorphic type have advanced substantially and have been framed with a more complete basis over the past 20 years. In such models, complete distributions of dislocation lines are not tracked nor can they be extracted. GC crystal plasticity models have limitations on length and time scales only by virtue of computational complexity relative to local continuum theory owing to additional degrees of freedom. For purposes of the present discussion, we consider two classes of GC crystal plasticity models

- Plastic strain gradient (slip gradient) crystal plasticity theory, with focus on the standard generalized thermodynamic formulation of slip gradient theory proposed by Gurtin [51] as the canonical exemplar.
- Micromorphic crystal plasticity, with focus on a more simplified micropolar theory as a subset [66, 70, 149].

Owing to close parallels (with some differences) of these two frameworks [68, 70], in the next section we outline a model for micropolar crystal plasticity to serve as a basis for overlapping bottom−up and top−down GC models in concluding remarks.

6. Mesoscopic Dislocation Density-Based Micropolar Model for Submicron Crystal Plasticity

The linkages between the micromorphic continuum and metal plasticity were recognized very early by Claus and Eringen [150] and Eringen and Claus [138]. We may choose to include both micro-rotations and stretch of director vectors associated with the lattice to pursue a so-called micromorphic description of crystal plasticity [64], or only the microrotations (so-called micropolar crystal plasticity). Significant advances in interpreting Cosserat crystal plasticity [151, 152] led to more complete micropolar crystal plasticity models [66−70] and micromorphic [61−64, 153] models framed as non-local extensions of crystal plasticity. Micropolar theory has the advantage that it does not require gradient or curl operations on the plastic deformation. Micropolar crystal plasticity [66, 70]is capable of predicting scale- and dislocation configuration-dependent mechanical behavior in single crystals [67, 69], maintains the "standard" treatment of elastic-plastic thermodynamics within the context of a higher order work-conjugate thermodynamic approach, requires fewer nodal DOF than slip gradient-based approaches to crystal plasticity, and allows the use of standard C^0-continuous shape functions to incorporate rotation of the lattice director vector. Relatively simple physically-based micropolar crystal plasticity models can capture sub-micron size effects in plasticity via incorporation of elastic torsion-curvature and an evolution equation for the plastic torsion-curvature, expressing a yield potential or flow rule as a combined, single function of the resolved slip system shear stress and couple-stresses conjugate to GNDs of screw and edge type. For this reason, the micropolar model receives emphasis here. In these models, dislocation evolution distinguishes between GNDs and statistically stored dislocations (SSDs), and the slip system back stress is naturally related to the skew symmetric part of the Cauchy stress. Mayeur and McDowell [68] demonstrated close parallels between the structure of micropolar crystal plasticity presented here and Gurtin's slip gradient model [51], apart from differences in identification of energetic and dissipative length scales and decompositions of stress and inelastic strain. Higher order boundary conditions differ as well, and Forest *et al.* [64] argue that micromorphic crystal plasticity can provide more flexibility in this regard since the micropolar theory neglects microstretch.

We next summarize the structure of micropolar crystal plasticity within the context of linearized kinematics, both for simplicity of presentation and because the model can be applied in this regime to overlap with bottom−up simulations to facilitate parameter estimation. For the most part, we follow the model framework set forth in complete detail by Mayeur *et al.* [70]. In the following, overbars indicate micropolar kinematic quantities. In the case of linearized kinematics, the displacement gradient is split into elastic distortion and plastic distortion

$$\mathbf{u}\nabla = \mathbf{H} = \mathbf{H}^{\mathrm{e}} + \mathbf{H}^{\mathrm{p}}. \tag{1}$$

Identifying the distortion components in this case with respective micropolar elastic and plastic strains gives

$$\bar{\boldsymbol{\varepsilon}} = \mathbf{u}\overleftarrow{\nabla} - \bar{\boldsymbol{\Phi}} = \bar{\boldsymbol{\varepsilon}}^{\mathrm{e}} + \bar{\boldsymbol{\varepsilon}}^{\mathrm{p}} = \boldsymbol{\varepsilon}^{\mathrm{e}} + (\boldsymbol{w}^{e} - \bar{\boldsymbol{\Phi}}) + \bar{\boldsymbol{\varepsilon}}^{\mathrm{p}}, \tag{2}$$

$$\bar{\boldsymbol{\kappa}} = \bar{\boldsymbol{\phi}}\,\overleftarrow{\nabla} = \bar{\boldsymbol{\kappa}}^{\mathrm{e}} + \bar{\boldsymbol{\kappa}}^{\mathrm{p}}. \tag{3}$$

The three components of microrotation vector $\bar{\boldsymbol{\phi}}$ are considered as additional degrees of freedom in the micropolar model, augmenting three displacement degrees of freedom. Here, $\boldsymbol{w}^{e}$ is the lattice rotation associated with the micropolar elastic strain and $\bar{\boldsymbol{\Phi}}$ is the 2nd rank microrotation tensor with components expressed in terms of its dual vector $\bar{\boldsymbol{\phi}}$, i.e., $\bar{\Phi}_{ij} = -e_{ijk}\bar{\phi}_k$, where the permutation tensor components are identified as e_{ijk}. While Mayeur *et al.* [70] have outlined the context of finite strain kinematics and anisotropic lattice elasticity, for simplicity we present here the stress−strain relation for the special case of isotropic linear elasticity

$$\boldsymbol{\sigma} = \lambda \mathrm{tr}(\bar{\boldsymbol{\varepsilon}}^{\mathrm{e}})1 + 2\mu\ \mathrm{sym}(\bar{\boldsymbol{\varepsilon}}^{\mathrm{e}}) + 2\mu_c\ \mathrm{skw}(\bar{\boldsymbol{\varepsilon}}^{\mathrm{e}}), \tag{4}$$

where λ and μ have their usual interpretation as Lamé constants, the latter as shear modulus. This relation can be expressed in terms of the standard symmetric small elastic strain tensor $\boldsymbol{\varepsilon}^{\mathrm{e}}$ as

$$\boldsymbol{\sigma} = \lambda \mathrm{tr}(\boldsymbol{\varepsilon}^{\mathrm{e}})1 + 2\mu\boldsymbol{\varepsilon}^{\mathrm{e}} + 2\mu_c(\boldsymbol{w}^{e} - \bar{\boldsymbol{\Phi}}). \tag{5}$$

The couple stress−elastic torsion lattice-curvature relation is given by

$$\mathbf{m} = \alpha \mathrm{tr}(\bar{\boldsymbol{\kappa}}^{\mathrm{e}})1 + 2\beta\ \mathrm{sym}(\bar{\boldsymbol{\kappa}}^{\mathrm{e}}) + 2\gamma\ \mathrm{skw}(\bar{\boldsymbol{\kappa}}^{\mathrm{e}}). \tag{6}$$

In this formulation, the Cauchy stress is non-symmetric. Non-standard micropolar elastic constants (i.e., not found in classical

local isotropic linear elasticity) include μ_c, α, β and γ. The non-classical elastic constant, μ_c, serves as an internal penalty constraint used to force the lattice rotation to closely approximate the rotational part of the elastic distortion, leading to the identification of the micropolar torsion-curvature with the lattice torsion-curvature

$$\mathrm{skw}(\bar{\boldsymbol{\varepsilon}}^{\mathrm{e}}) = \mathrm{skw}(\mathbf{H}^{\mathrm{e}} - \bar{\boldsymbol{\Phi}}) = \boldsymbol{\omega}^{\mathrm{e}} - \bar{\boldsymbol{\Phi}} \approx \mathbf{0} \Rightarrow \boldsymbol{\omega}^{\mathrm{e}} \approx \bar{\boldsymbol{\Phi}}. \tag{7}$$

This facilitates a direct connection between GNDs and associated scale effects within this framework, as well as direct parallels with slip gradient crystal plasticity. It should be borne in mind that the ratio μ_c/μ should be large ($\sim$ factor of 10) but not infinite; otherwise, nonsymmetric Cauchy stress would be precluded, and this component of stress directly gives rise to slip system back stress that is critical in modeling size effects.

Elastic (energetic) length scales can be defined as $\ell_{e1} = \sqrt{\alpha/\mu}$, $\ell_{e2} = \sqrt{\beta/\mu}$ and $\ell_{e3} = \sqrt{\gamma/\mu}$, and introduce micropolar effects associated with elastic torsion-curvature (effectively coupled in elastic-plastic flow slip gradients via the decomposition in Eq. (2)).

The conjugacy of $\mathbf{m} - \bar{\boldsymbol{\kappa}}$ augments the stress–strain conjugacy found in standard thermodynamics. The thermodynamically consistent framework is laid out in Mayeur *et al.* [70]. In the absence of body forces and couples, balance of both linear and angular momentum must be satisfied

$$\nabla \cdot \boldsymbol{\sigma}^T = \mathbf{0}, \tag{8}$$

$$\nabla \cdot \mathbf{m}^T - \mathbf{e} : \boldsymbol{\sigma} = \mathbf{0}. \tag{9}$$

We further assume that the micropolar plastic strain rate is the plastic distortion rate

$$\dot{\bar{\boldsymbol{\varepsilon}}}^{\mathrm{p}} = \dot{\mathbf{H}}^{\mathrm{p}} = \sum_{\alpha} \dot{\gamma}^{\alpha} \mathbf{s}^{\alpha} \otimes \mathbf{n}^{\alpha}. \tag{10}$$

The micropolar plastic strain rate includes both the symmetric and skew-symmetric parts of the plastic distortion rate.

In this model, as per Forest *et al.* [154], we assign evolution equations for the plastic torsion-curvature that relate directly to the rate of evolution of edge and screw GNDs

$$\dot{\bar{\boldsymbol{\kappa}}}^{\mathrm{p}} = \sum_{\alpha} \left[\frac{\dot{\varphi}^{\alpha}_{\perp}}{L^{\alpha}_{\perp}} \mathbf{t}^{\alpha} \otimes \mathbf{s}^{\alpha} + \frac{\dot{\varphi}^{\alpha}_{\odot}}{L^{\alpha}_{\odot}} \left(\mathbf{s}^{\alpha} \otimes \mathbf{s}^{\alpha} - \frac{1}{2} \mathbf{I} \right) \right] \tag{11}$$

with specific constitutive assignment of edge and screw GND terms, respectively, given by

$$\dot{\varrho}^{\alpha}_{G,\perp} = -\frac{\dot{\varphi}^{\alpha}_{\perp}}{b L^{\alpha}_{\perp}} \quad \text{and} \quad \dot{\varrho}^{\alpha}_{G,\odot} = -\frac{\dot{\varphi}^{\alpha}_{\odot}}{b L^{\alpha}_{\odot}}, \tag{12}$$

where $L^{\alpha}_{\perp}$ and $L^{\alpha}_{\odot}$ are so-called plastic length scales associated with edge and screw dislocations, respectively. They control the initial rate of hardening associated with the back stress. After Arsenlis and Parks [34], the total GND density and its rate are given by

$$\varrho^{\alpha}_{G} = \sqrt{(\varrho^{\alpha}_{G,\perp})^2 + (\varrho^{\alpha}_{G,\odot})^2}, \tag{13}$$

$$\dot{\varrho}^{\alpha}_{G} = \frac{1}{\varrho^{\alpha}_{G}} (\varrho^{\alpha}_{G,\perp} \dot{\varrho}^{\alpha}_{G,\perp} + \varrho^{\alpha}_{G,\odot} \dot{\varrho}^{\alpha}_{G,\odot}). \tag{14}$$

In two-dimensional (2D) plane strain problems involving only geometrically necessary edge dislocations, screw dislocations play no role and so only $L^{\alpha}_{\perp}$ is relevant. We assume generalized normality and its unconditional satisfaction of the strong form of the Clausius–Duhem 2nd law inequality, adopting a flow potential or yield function for each slip system of the form

$$F^{\alpha} = \hat{\tau}^{\alpha} - (r^{\alpha}_{o} + r^{\alpha}) \leq 0, \tag{15}$$

where

$$\hat{\tau}^{\alpha} = \sqrt{|\tau^{\alpha}_{\mathrm{eff}}|^2 + |\pi^{\alpha}_{\perp}/L^{\alpha}_{\perp}|^2 + |\pi^{\alpha}_{\odot}/L^{\alpha}_{\odot}|^2} \tag{16}$$

and r^{α}_{o} and r^{α} are the slip system level initial and evolving athermal threshold stress components, respectively.

The effective shear stress and resolved couple stresses for edge and screw dislocation populations are given by

$$\tau^{\alpha}_{\mathrm{eff}} = \boldsymbol{\sigma} : (\mathbf{s}^{\alpha} \otimes \mathbf{n}^{\alpha}), \tag{17}$$

$$\pi^{\alpha}_{\perp} = \mathbf{m} : (\mathbf{t}^{\alpha} \otimes \mathbf{s}^{\alpha}), \tag{18}$$

$$\pi^{\alpha}_{\odot} = \mathbf{m} : \left(\mathbf{s}^{\alpha} \otimes \mathbf{s}^{\alpha} - \frac{1}{2} \boldsymbol{I} \right). \tag{19}$$

It follows from generalized normality that

$$\dot{\bar{\boldsymbol{\varepsilon}}}^{\mathrm{p}} = \sum_{\alpha} \dot{\lambda}^{\alpha} \frac{\partial F^{\alpha}}{\partial \boldsymbol{\sigma}} \quad \text{and} \quad \dot{\bar{\boldsymbol{\kappa}}}^{\mathrm{p}} = \sum_{\alpha} \dot{\lambda}^{\alpha} \frac{\partial F^{\alpha}}{\partial \mathbf{m}}. \tag{20}$$

We adopt a power law for the viscoplastic multiplier to express the shearing rates and GND densities driving the plastic torsion-curvature on all slip systems as

$$\dot{\gamma}^{\alpha} = \dot{\lambda}_0 \left(\frac{\langle \hat{\tau}^{\alpha} - (r^{\alpha}_{o} + r^{\alpha}) \rangle}{g^{\alpha}} \right)^{m} \frac{\tau^{\alpha}_{\mathrm{eff}}}{\hat{\tau}^{\alpha}}, \tag{21}$$

$$\dot{\varphi}^{\alpha}_{\perp} = \dot{\lambda}_0 \left(\frac{\langle \hat{\tau}^{\alpha} - (r^{\alpha}_{o} + r^{\alpha}) \rangle}{g^{\alpha}} \right)^{m} \frac{\pi^{\alpha}_{\perp}/L^{\alpha}_{\perp}}{\hat{\tau}^{\alpha}}, \tag{22}$$

$$\dot{\varphi}^{\alpha}_{\odot} = \dot{\lambda}_0 \left(\frac{\langle \hat{\tau}^{\alpha} - (r^{\alpha}_{o} + r^{\alpha}) \rangle}{g^{\alpha}} \right)^{m} \frac{\pi^{\alpha}_{\odot}/L^{\alpha}_{\odot}}{\hat{\tau}^{\alpha}}. \tag{23}$$

Here, g^{α} is a viscous drag stress, and the athermal threshold stress is given by

$$r^{\alpha} = c_1 \mu b \sqrt{\sum_{\beta} h^{\alpha\beta} \varrho^{\beta}_{S}}, \tag{24}$$

where ϱ^{β}_{S} is the SSD density ascribed to slip system β, and $h^{\alpha\beta}$ are hardening coefficients. As pointed out by Mayeur *et al.* [70], prior comparisons to DDD simulations have shown that by assigning *a priori* dependence of r^{α} on GND density in micropolar theory significantly overestimates the strengthening, likely owing to the natural incorporation of back stress into $\hat{\tau}^{\alpha}$ via $\tau^{\alpha}_{\mathrm{eff}}$, as discussed shortly. This differs substantially from the approach taken in GC plasticity models that attribute enhanced hardening effects of GNDs to the evolving threshold stress r^{α}. In our view, it will not be possible to faithfully model dislocation phenomena in nanostructured multilayers and other similar systems with this latter kind of GC approach.

In this framework, as also the case for slip gradient theories, effects of initial threshold slip system yield strength, r^{α}_{0}, are not expressed in terms of GND densities and may depend on the initial dislocation source distribution as well as obstacles and interfaces that impede slip. Rys *et al.* [153] included GND dependence in the initial CRSS of slip systems in a micromorphic crystal plasticity model. The role of the stress gradient on dislocation nucleation was first addressed by Miller and Acharya [155]. Chakravarthy and Curtin [156] contributed to understanding the effects of the stress gradient on yield stress for dislocation interaction with obstacles using discrete

dislocation theory and formalized the approach in GC plasticity. The concept was later applied to modeling of fracture using DDD [157]. GC crystal plasticity models that include both stress and strain gradient effects have been introduced [158, 159]. It is understood that stress gradients manifest size effects of initial yield stress due to pile-ups at barriers, while strain gradients manifest size effects in work hardening associated with GND configurations, so it would be presumed that an initial GND state would have existed via, prior deformation or thermomechanical processing. In comparison to DDD solutions for micron scale field problems, we have found r_0^α to correlate with a mean free path length for the initial configuration of GNDs [69], but do not expect this to be a general result.

SSD density corresponds to the component of dislocation density having no net Burgers vector over a given volume/Burgers circuit, and its evolution relations are distinct from that of GND densities. For example, we can follow the approach of Mecking and Kocks [160]

$$\dot{\varrho}_S^\alpha = \frac{1}{b}\left(\frac{1}{l^\alpha} - 2y_c\varrho_S^\alpha\right)\dot{\lambda}^\alpha, \tag{25}$$

where y_c is the dislocation annihilation distance, and the mean free path given by

$$l^\alpha = \frac{K}{\sqrt{\sum_\beta a^{\alpha\beta}\varrho_S^\beta}} \tag{26}$$

with K as an average dislocation junction strength with interaction matrix $a^{\alpha,\beta}$. The plastic multiplier is given by

$$\dot{\lambda}^\alpha = \sqrt{|\dot{\gamma}^\alpha|^2 + |\dot{\varphi}_\perp^\alpha|^2 + |\dot{\varphi}_\odot^\alpha|^2}. \tag{27}$$

As mentioned by Mayeur *et al.* [70], the evolution of SSD density is driven by $\dot{\lambda}^\alpha$ rather than slip system shearing rates $\dot{\gamma}^\alpha$ alone, resulting in scale dependent isotropic hardening that was found to better mimic DDD simulations.

The effective shear stress is given by

$$\tau_{\text{eff}}^\alpha = \mathbf{s}^\alpha \cdot \boldsymbol{\sigma} \cdot \mathbf{n}^\alpha = \mathbf{s}^\alpha \cdot [\text{sym}(\boldsymbol{\sigma}) + \text{skw}(\boldsymbol{\sigma})] \cdot \mathbf{n}^\alpha. \tag{28}$$

Alternatively, this can be written as

$$\tau_{\text{eff}}^\alpha = \tau^\alpha - \tau_b^\alpha, \tag{29}$$

$$\tau^\alpha = \mathbf{s}^\alpha \cdot \text{sym}(\boldsymbol{\sigma}) \cdot \mathbf{n}^\alpha \quad \text{and}$$
$$\tau_b^\alpha = -\mathbf{s}^\alpha \cdot \text{skw}(\boldsymbol{\sigma}) \cdot \mathbf{n}^\alpha = -\frac{1}{2}\mathbf{t}^\alpha \cdot (\nabla \cdot \mathbf{m}^T). \tag{30}$$

The slip system back stress therefore emerges naturally as the skew symmetric Cauchy stress resolved onto the slip system; it is subtracted in Eq. (29) from the classical resolved shear stress based on the symmetric part of Cauchy stress. In Eq. (30), $\mathbf{t}^\alpha = \mathbf{s}^\alpha \times \mathbf{n}^\alpha$, and the last term arises from balance of angular momentum in the absence of body couples. The slip system back stress is directly linked to lattice torsion-curvature gradients, taken in conjunction with Nye's relation [161]; this is in direct analogy to Gurtin's slip gradient theory [51].

Compatibility in this case of linearized kinematics is given by

$$\text{curl}(\mathbf{u}\nabla) = \mathbf{0}. \tag{31}$$

The dislocation density tensor α is defined by

$$\boldsymbol{\alpha} = -\text{curl}(\mathbf{H}^e) = \text{curl}(\mathbf{H}^p) \tag{32}$$

and can be related to slip gradients via

$$\boldsymbol{\alpha} = \sum_\alpha \varrho_{G\perp}^\alpha \mathbf{b}^\alpha \otimes \mathbf{t}^\alpha + \varrho_{G\odot}^\alpha \mathbf{b}^\alpha \otimes \mathbf{s}^\alpha, \tag{33}$$

where the slip gradients projected onto the glide directions are defined as

$$\varrho_{G\perp}^\alpha = -\frac{1}{b}\nabla\gamma^\alpha \cdot \mathbf{s}^\alpha \quad \text{and} \quad \varrho_{G\odot}^\alpha = \frac{1}{b}\nabla\gamma^\alpha \cdot \mathbf{t}^\alpha. \tag{34}$$

As mentioned earlier, the lattice torsion-curvature relations in micropolar theory not only depend on the tensor $\boldsymbol{\alpha}$, but also involve the elastic lattice torsion-curvature, the last term on the RHS in the expression

$$\boldsymbol{\kappa} = -\boldsymbol{\alpha}^T + \frac{1}{2}\text{tr}(\boldsymbol{\alpha})\mathbf{I} + [\text{curl}(\boldsymbol{\varepsilon}^e)]^T. \tag{35}$$

We note that the first two terms on the RHS in Eq. (35) are classical terms that arise in slip gradient theory [161, 162]. The elastic torsion-curvature is added within the micropolar framework and is assigned as a state variable in the thermodynamic free energy.

Additional Neumann and/or Dirichlet microboundary conditions must be specified for the microtraction vector $\mathbf{M}$ associated with couple stress $\mathbf{m}$ and the dual vector for microrotation, $\bar{\phi}$

$$\mathbf{M} = \mathbf{m} \cdot \mathbf{n} = \mathbf{M}^* \text{ on } \partial R_m, \tag{36}$$

$$\bar{\boldsymbol{\phi}} = \bar{\boldsymbol{\phi}}^* \text{ on } \partial R_{\bar{\phi}}. \tag{37}$$

In many problems, a microhard condition $\bar{\boldsymbol{\phi}} = \mathbf{0}$ can be applied, or one can simply assert continuity of fields of microrotation across domains or periodic boundaries, depending on the problem. Both slip gradient plasticity (dislocation flux) and micromorphic plasticity theory have more generality in this regard, but nonetheless physical interpretations of higher order boundary conditions remains a challenge for these GC crystal plasticity models; hence, minimization of complexity is desirable. We remark that dislocation flux relations for interfaces are challenging not only for GC models, but even for bottom−up DDD models; recent progress is being made in coupling information from atomistics to inform dislocation−grain boundary interactions [163], but this is a very high dimensionality problem that likely will require application of data science methods to advance significantly. Moreover, as discussed earlier, even atomistic models are not immune to uncertainty in their prediction of dislocation reactions at interfaces owing to multiple issues such as free volume, changes of electronic structure owing to disorder and free volume, empiricism in potentials, etc.

7. 2D Plane Strain Field Problems for Micropolar Crystal Plasticity

We next briefly highlight the application of the foregoing micropolar crystal plasticity framework to 2D plane strain dislocation field initial-boundary value problems that facilitate direct comparison with DDD simulations. Along these lines, Mayeur and McDowell [66, 67, 69] have shown that micropolar crystal plasticity can effectively mimic DDD type solutions for bending of single crystal thin films, simple shear of constrained thin films, and particle strengthening, respectively. The micropolar model was independently calibrated for each boundary value problem by fitting to both average (e.g., stress−strain curves) and microscopic (e.g., dislocation density distributions) deformation behavior. It was demonstrated in an early work [149] that fitting to multiple aspects of the

deformation behavior is necessary to obtain a unique set of micropolar constitutive parameters. Across all applications for single crystal Al, the linear elasticity is idealized as isotropic with a shear modulus and Poisson's ratio of 26.3 GPa and 0.33, respectively. The couple modulus μ_c is assigned as 263 GPa for all cases, a factor of 10 greater than μ. The Burgers vector is fixed in magnitude at 0.25 nm. Drag stress g^α and inverse rate sensitivity m are fixed at 5 MPa and 20, respectively, for all applications. Effectively, parametric simulations are conducted to consider couple stress constants and GND related parameters ℓ_e, $L_p = L_\perp^\alpha$, along with the initial threshold stress r_o to correlate micropolar theory with DDD simulations. For some problems, the hardening matrix $h^{\alpha\beta}$ (along with initial SSD density) and dislocation interaction matrix $a^{\alpha\beta}$ are employed, while for others only GNDs are assumed to exist. The interested reader can refer to Refs. 66, 67, 69 and 70 for more details.

An example of the application of micropolar crystal plasticity to shear of a 1-μm thick constrained thin film of single crystal aluminum is shown in Fig. 8. The film is oriented for symmetric slip with thickness, $H = 1\,\mu$m. Only edge dislocations are considered [67]. The upper and lower surfaces are constrained against vertical displacement, impenetrable to dislocations in the DDD simulations, and treated with microhard boundary conditions in the micropolar model. The fits and are in good agreement with the discrete dislocation results. Fit 1 uses slightly higher threshold hardening (mean free path coefficient $K_1 = 16.67$ versus $K_2 = 18.18$), whereas fit 2 has a larger contribution from gradient kinematic hardening ($\ell_e = 15$ nm versus $\ell_e = 10$ nm for fit 1). The plastic length scales of both fits were assumed as 45 nm. The hardening and interaction matrices for SSD effects were assumed to follow the simple form $h^{\alpha\beta} = a^{\alpha\beta} = \delta^{\alpha\beta}$. Comparison of the shear strain distributions shown in Fig. 8 shows relatively close agreement with DD simulations of Shu *et al.* [164] as well.

Simulations of a submicron-scale particle reinforced aluminum matrix system subjected to 2D shear were conducted by Mayeur and McDowell [69] and are further illustrative of the capabilities of the micropolar model to mimic DDD. Here, comparisons are made with the DDD simulations of Yefimov *et al.* [165]. The periodic unit cell shown in Fig. 9 consists of stiff elastic ($\mu = 192.4$ GPa and $\nu = 0.33$)

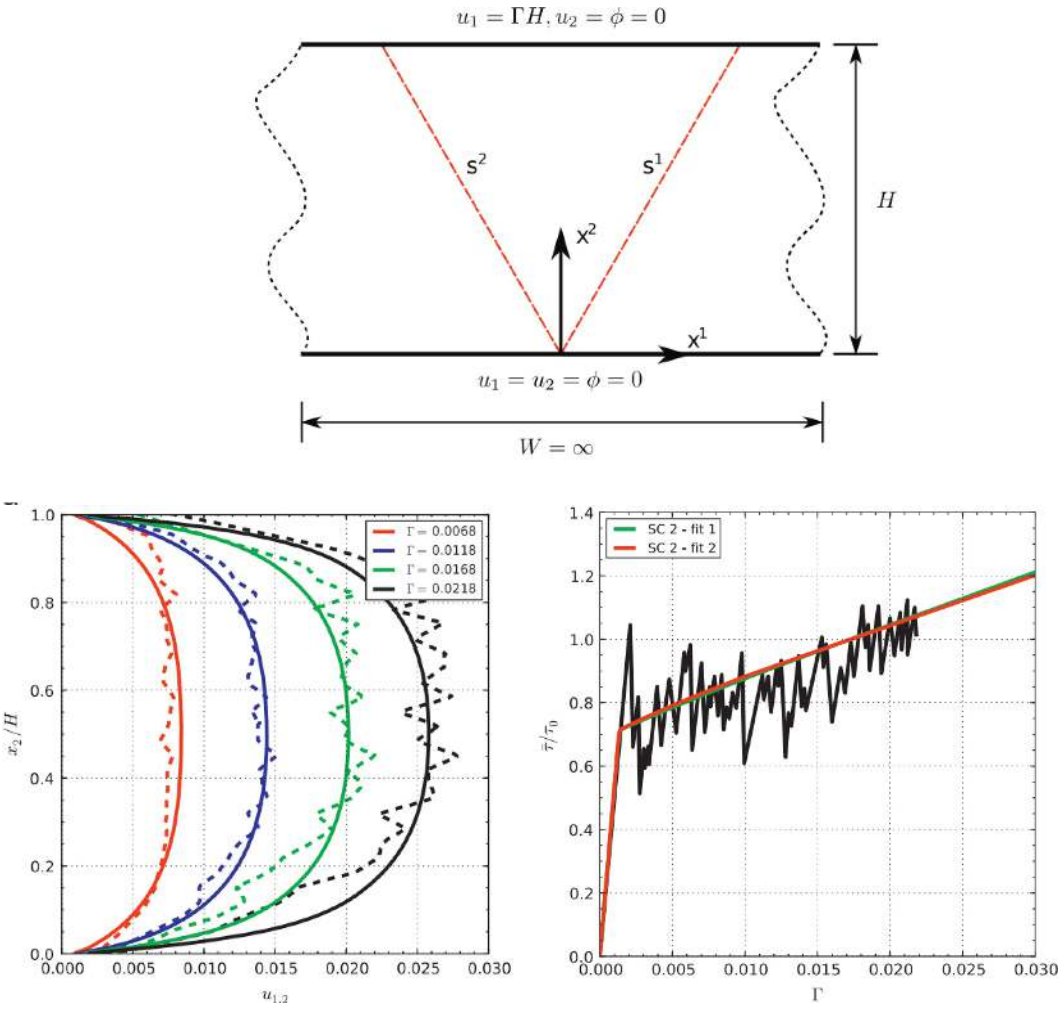

Fig. 8. (a) Geometry and boundary conditions for finite element analysis of planar double slip under imposed shear Γ of a constrained thin film using micropolar finite element simulations (simple single criterion strength model) for $H = 1\,\mu$m. Results for simulated shear strain distributions in solid lines across the cross section (b) are compared with (dashed lines) discrete dislocation modeling results [164] as a function of imposed simple shear, and (c) the micropolar simulations of average shear stress response as a function of the imposed shear Γ (solid lines) are compared with the discrete dislocation results (jerky trajectory) [67].

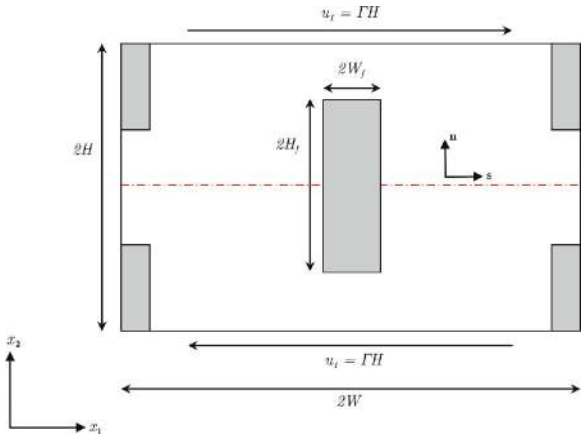

Fig. 9. Periodic unit cell (x_1 direction) for geometry and slip system configuration for the aluminum matrix–particle reinforced system in constrained shear [70].

particles arranged within a ductile single crystal. Single slip occurs in the x_1 direction. The elastic and plastic length scales are assigned as 125 nm. A range of cell sizes $H = 0.5C$, C, and $2C$ are considered, where $C = 4000b = 1\,\mu$m, since $b = 0.25$ nm for the aluminum matrix. Two cases are considered, labeled as Material I and Material II; they have the same particle area fraction, but Material I has square particles with $W_f = H_f = 0.416H$, providing a direct pathway for unobstructed slip. Material II has rectangular particles with $2W_f = H_f = 0.588H$, resulting in blockage of slip. The micropolar elastic constants (μ_c and β) for the inclusion and matrix phases are set equal as just one particular choice that simplifies the simulation. SSDs are excluded in the micropolar simulations, and accordingly no related hardening due to SSDs is incurred, nor can slip system interactions occur. The initial dislocation density was set to zero. For the DDD simulations, dislocation sources were randomly distributed and source strengths were determined by randomly sampling from a Gaussian distribution with a mean nucleation strength of 50 MPa and a standard deviation of 10 MPa.

The system is subjected to simple shear through displacement boundary conditions applied to top and bottom surfaces, and these surfaces are assumed to be couple stress traction free. Periodic boundary conditions are enforced on displacements and microrotation at the left and right surfaces. The average overall shear stress–strain response of the unit cell is shown in Fig. 10(a). We clearly observe the blocking effect of the particles resulting in strain hardening for Material II and essentially perfectly plastic behavior for Material I, with its unlimited mean free path for slip in the x_1 direction. The strengthening in Material II is governed by the development of back stress, as evidenced by the pronounced Bauschinger effect, while unloading is essentially elastic for Material I. The average stress–strain curves predicted by the micropolar model (solid lines in Fig. 10(a) are in good agreement with the discrete dislocation results during forward loading; however, the Bauschinger effect for Material II is significantly overstated, perhaps owing to differences in details of the DDD and micropolar models, as well as the assigned equality of higher order constants at the particle–matrix interface. As pointed out by Mayeur *et al.* [70], it is assumed that the lattice rotations at the matrix–particle interface are equal and therefore the finite element nodes along the matrix–particle interface are shared between the two materials. This represents a different boundary condition than what is enforced at the matrix–particle interface in the DDD simulation, one of the continuity of displacement and zero slip at the vertical particle–matrix interfaces. The micropolar constants in each phase can be modified to explore improvement in correlation by modifying microrotation across the interface. It is also remarked that the micromorphic crystal plasticity formulation has yet more DOF in specifying these interface conditions owing to the inclusion of microstretch along with microrotation, see e.g., Refs. 64 and 153.

Figure 10(b) shows the average shear stress–strain curves for Material II for three different unit cell sizes. We found that it was necessary to use different r_o values to obtain good agreement with the discrete dislocation results; the calibrated values of r_o for the three cases (13, 21 and 30 MPa, respectively) show strong correlation with a standard Hall–Petch relation for r_o based on the initial mean free slip length for each case. Cumulative plastic slip and dislocation density also compare well between the micropolar and DDD simulations [70].

We note that the micropolar crystal plasticity simulations outlined here have considered 2D deformation for submicron-scale problems with simple boundary conditions for which size effects are pronounced. Of course, the 2D case is a simplification to facilitate comparison with DDD, focusing on edge dislocation populations of GNDs. The reader will note that a significant fraction of the structure of the micropolar crystal plasticity parallels advanced

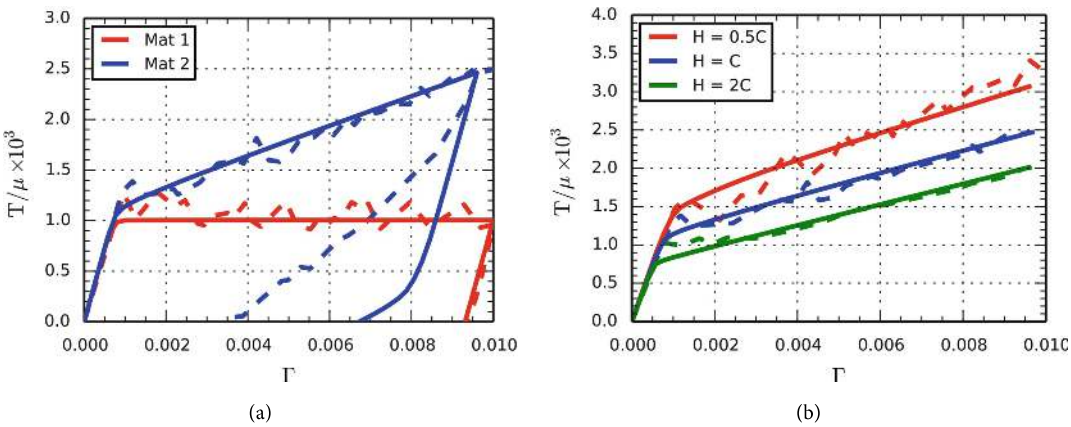

Fig. 10. Average shear stress–strain response for (a) Materials I and II for $H = C$ and (b) Material II with variable slip threshold for different particle spacings for the same particle area fraction. Dashed lines represent discrete dislocation results [165] and solid lines are micropolar results [70].

dislocation density-based crystal plasticity approaches of local type, with many parameters in common. The total number of such common parameters is limited and most can be informed to lie within some reasonable range on a physical basis. For this reason, such approaches are preferred over more abstract reduced order frameworks. However, the number of parameters associated with the additional DOF of these GC crystal plasticity models increases as we move to 3D problems. The foregoing 2D plane strain comparisons between DDD and micropolar crystal plasticity have assumed isotropic linear elasticity, a single elastic length scale $\ell_e = \ell_{e2} = \ell_{e3}$, and a single plastic length scale $L_p = L_{\perp}^{\alpha}$ since screw dislocations need not be considered. Moreover, all make the estimate $\mu_c \approx 10\,\mu$. The primary parameters involved in fitting DDD simulations in such cases are the set $\{r_o, K, \ell_e, L_p\}$. This enables traditional parametric study of parameter sensitivity and identification of higher order parameters. In the 3D case of micropolar crystal plasticity for isotropic linear elasticity, these include

- Elastic length scales: $\ell_{e1} = \sqrt{\alpha/\mu}$, $\ell_{e2} = \sqrt{\beta/\mu}$ and $\ell_{e3} = \sqrt{\gamma/\mu}$
- Plastic length scales: $L_{\perp}^{\alpha}$ and $L_{\odot}^{\alpha}$
- Couple modulus: μ_c

Clearly, the 3D case requires a more complete set; moreover, consideration of anisotropic elasticity for crystals would increase the number of elastic constants (and associated length scales) considerably. Accordingly, extension to 3D can appear daunting. However, the attractive feature of micropolar crystal plasticity remains that only three additional DOF (microrotation vector) need be considered, and these are subject to ordinary FE interpolation schemes. There is no need to evaluate slip gradient or curl operations. Moreover, the micromorphic crystal plasticity theory adds only the microstretches. One must then ask whether the machinery of slip gradient plasticity leads to far superior specification of interface and interface boundary conditions than these GC models. The answer is not certain in all cases.

In the next section, we suggest a methodology that may preserve some of the desirable aspects of the micropolar crystal plasticity model framework, building on parameter estimation by comparison with DDD simulations considered to this point, and extending in some fundamental ways via CG atomistics. Moreover, inference-based data science methods can be exploited to assist in estimation of higher order micropolar model parameters, interface conditions, and boundary conditions. Similar comments would apply, of course, to the estimation of additional parameters related to slip gradient models.

8. Bridging Bottom–Up Models to Reduced Order GC Crystal Plasticity Models: Prospectus

Parameter identification/estimation and interpretation of higher order boundary conditions is one of the challenges of thermodynamically consistent GC crystal plasticity models, including micromorphic and micropolar crystal plasticity, since they involve additional DOF and additional boundary conditions that may lack clear physical interpretation. However, it should be borne in mind that any nonlocal GC model leads to such complications. Moreover, atomistic simulations and DDD simulations have similar limitations in terms of applying boundary conditions that seek to faithfully represent physical experiments. In the micropolar model, elastic (energetic) material length scales are introduced via the couple stress elastic constants and plastic (dissipative) length scales are introduced in the flow rule. We may distinguish characteristic elastic length scales associated with dilatation and shear relative to lattice orientation even for isotropic linear elasticity, unlike slip gradient theory. Moreover, screw and edge dislocations in micropolar theory have distinct characteristic length scales in affecting lattice torsion-curvature. These length scales can potentially be estimated via calibration to bottom−up models (CAC) that has long-range field interactions and full (elastic and plastic) lattice curvature. That being said, elastic and plastic length scales that normalize micropolar elastic constants and slip gradient terms may depend on specific initial-boundary value problems of interest, since these models are of reduced order nature and do not have the capability to distinguish between higher order spatial statistics of dislocation configurations. It is unrealistic to think of them as material constants or fixed parameters. Accordingly, a similar strategy can be pursued wherein a number of different experimental configurations with associated strain gradients can be considered, e.g., torsion of thin wires [145, 147], nanoindentation [148], specimens with various notch radii, etc., to establish parameter estimates that relate to applications of interest. Without such top−down information, avenues for parameter estimation are limited.

It should be borne in mind that GC crystal plasticity theories of slip gradient type or micropolar/micromorphic type are by definition limited to low order representations of higher order spatial statistics of dislocations and to linearization of lattice hyperelasticity. A bottom−up CG atomistic model such as CAC is useful to inform the mesoscale micropolar model for the following reasons:

- The underlying elastic potential is hyperelastic (solely based on the interatomic potential) and the kinematics are general; hence, CG atomistic simulations can be employed to estimate micropolar elastic constants and length scales using simulations that impose lattice curvature. This is similar to ideas set forth by Luscher *et al.* [166] to estimate elastic constants in GC models for defected media subjected to higher order deformation modes (e.g., twist and gradient stretching). As a result, the estimation of elastic length scales can be systematically approached by considering distinct higher order deformation modes that solicit different respective modes of lattice curvature. This can also be performed via application of CG atomistics to lattices with pre-assigned GNDs and associated plastic curvature. As elastic length scales are typically smaller than plastic length scales, this can also engender some understanding of how these scales may evolve as a function of GND density. Since the elastic length scales reckoned for the micropolar model based on comparison to DDD have been on the order of tens to a few hundred nm, presumably CG atomistic simulations can be conducted that are sufficiently large to explore them, as well as degree of coupling with pre-existing GND arrays. Since elastic curvature is a consideration only for micromophic and micropolar theories, it can be considered as an aspect that is distinct from slip gradient theories. It may be interesting to consider implications.
- Plastic length scales can be explored for somewhat higher domain sizes, also using comparisons to DDD simulations.
- Couple stress at mesoscales in such a model can be explored on the basis of both near core interactions of dislocations in close proximity (short-range) and long-range polarity of stress field interactions of sub-populations with different net Burgers vector. The former might have consequence at higher dislocation density. It is directly related to elastic lattice torsion-curvature and is relieved/accommodated by plastic curvature. It may be the case that the micropolar curvature-related length scales for low and high GND densities differ in ways that could be explored via

extended atomistics. These capabilities of CG atomistics resonate with the micropolar framework.
- No assumptions are made in CAC regarding dislocation junction strengths, generation of dislocations from sources, or work hardening parameters.

Bottom−up DDD simulations are useful in complementary manner to inform the mesoscale micropolar model

- DDD simulations can consider larger mesoscales (e.g., up to a few microns) encompassing substantial populations of dislocations, including both SSDs and GNDs.
- DDD simulations can more reasonably reflect finite temperature dislocation mobility and thermally-assisted dislocation generation and junction formation-breaking aspects, albeit by necessity resorting to certain *ad hoc* representations of these processes/mechanisms. Hence, certain slip system kinetics parameters of GC crystal plasticity models can potentially receive useful information. Of course, experiments are the typical benchmark for informing kinetics.
- Back stress acting on populations of dislocations can be computed via sorting out of long-and short-range elastic interactions of dislocations, so its prominent role in field problems involving dominance of GNDs can be assessed and used to inform micropolar models. In this way, plastic length scales affect strengthening for different characteristic classes of problems (e.g., multilayers, particle reinforcement, polycrystals, etc.) that can be considered.
- The dependence of the initial slip yield strength on dislocation mean free path and source spacing can be readily investigated by initial assignment of dislocations and sources, which is much easier to explore parametrically using DDD than CG-atomistics.

Finally, we comment that it is unlikely that the kinds of manual comparisons we have outlined in the 2D micropolar-DDD parameter studies will be the desired methodology as we move into the future. Use of data science (e.g., machine learning (ML)) techniques to fuse information from top−down experiments with these bottom−up models to inform GC crystal plasticity models in the presence of uncertainty is essential. In contrast to historical pathways, we do not over-emphasize the input from physical experiments, as their interpretation often effectively involves adoption of a reduced order model used to interpret their results, as well as uncertainty arising from imposed boundary conditions, measurement error, limitations on spatial and temporal resolution, etc. Moreover, physical experiments are costly. The highest utility experiments will include limited bulk specimens with more emphasis on *in situ* measurement methods that target highly uncertain model information/parameters, details of behavior at material interfaces or at other boundaries, full field information, etc. There is one contemporary line of argument that by resolving experimental measurements to scales approaching tens of nanometer and storing enormous amounts of information concerning evolution of GND density, etc., it may be possible to inform GC crystal plasticity models directly. While this could be true to some extent, the interpretation of these experimental data relies on model assumptions similar to those made in DDD and further exploits temporal and spatial averaging, either explicitly or implicitly. It is challenging to see a clear path forward to distinguish experiments involving elastic and plastic lattice torsion-curvature, given the expense associated with very different *in situ* experimental protocols to explore consideration of additional DOF in GC models; the relatively lower costs of CG atomistics and DDD might argue for their utility in forming the "backbone" of assessment of model form and parameter uncertainty in GC crystal plasticity models.

Naturally, physical experiments are preferred for their support of kinetics of nonequilibrium processes and estimate of the first-order model parameters, as has been exploited extensively in the past for local crystal plasticity models. Moreover, physical experiments have a way of shedding light on the efficacy of certain simplifying but erroneous assumptions that can be made in GC models, such as assigning elastic and plastic length scales summarily as "material constants" independent of the initial-boundary value problem.

We close this section with a brief set of suggestions for estimating parameters in GC crystal plasticity models based on reconciliation of bottom−up input from CG-atomistics and DDD simulations, as well as physical experiments, using micropolar crystal plasticity as a reference framework for GC models. We refer to experiments as "top−down" even if they resolve measurement of certain quantities at fine scale, since they are focused on (potentially) full field observations of selected field quantities and do not attempt to measure all discrete attributes (as in atomistics or CG atomistics or DDD simulations). This work highlights specific CG atomistics methods that extend to dislocation field problems and can address lower mesoscales of applicability of GC crystal plasticity models, overlapping with DDD models at the mesoscale; we trust that it may inspire future works in both estimation of parameters and forms of GC crystal plasticity models to improve their prospects for incorporation in toolkits of engineering analyses. The suggestions are as follows:

(1) Submicron-scale field problems dominated by GND effects are key to linking scale parameters of micropolar theory with bottom−up CAC and DDD model results. Field problems with dimension of the order of 1 μm with dislocations and heterogeneity that induce lattice curvature of both elastic and plastic nature are desirable. Reduction of ambiguity of boundary conditions and interface conditions is desirable (e.g., impenetrable boundaries and periodic boundaries). Examples may be found in prior DDD simulations and include
   (i) Plastic flow between plane parallel plates with various widths
   (ii) Torsional plastic flow of a constrained disk between parallel elastic plates
   (iii) Matrix flow through an array of periodic and non-periodic elastic phases with impenetrable interfaces, both 2D and 3D
   (iv) Indentation of a frictionless rigid surface (e.g., cone and sphere) on a deformable half space

(2) Uniaxial experimental data for elasticity and crystal plasticity of single crystals, when available, or of polycrystals, can assist with more standard crystal plasticity model parameter estimation, including kinetics and strain hardening beyond the dominate GND strengthening regime.

(3) ML approaches such as Gaussian process regression (GPR) with Bayesian inference and uncertainty estimation for surrogate models and for calibration of model parameters [167–169] can be used to consider information more objectively from bottom−up modeling methods in assessing likelihood of parameter estimates based on multiple sources of information. In moving from 2D to 3D simulations to support more complete parameter estimates for GC crystal plasticity models, the additional

parameter fitting/estimation can become overwhelmingly too complex to be undertaken based on human intuition. Limited traditional regression approaches are unlikely to yield useful estimates of pareto-optimal parameter sets for each type of application.

(4) Top–down experimental information can be fused with the bottom–up information, either via their incorporation in GPR or other ML scheme, or via some kind of weighted bottom–up and top–down strategy that considers uncertainty of information; either bottom–up information can be assigned weighted preference owing to less mesoscale uncertainty, or the notion of an interscale discrepancy layer can be introduced intended to capture any aspects of missing physics [170].

It is our view that the fusion of information from bottom−up model simulations with top−down experiments using advanced data science strategies will form the basis of a foundational and perhaps transformational advance in the understanding, quantification, identification, and application of GC crystal plasticity models in the coming decade. Much progress has been made in this regard just in the past 15 years owing only to high performance computing, largely absent contributions from advanced data science tools. With the addition of ML approaches, for example, new kinds of hierarchical multiscale parameter estimation schemes will emerge in the next decade. It is possible we will see the emergence of "smart" modeling platforms that learn to distinguish among model forms and parameters for different classes of characteristic modeling problems. Although this manuscript does not attempt to foray deeply into the realm of data science, some recent works give some insight into possible future directions for GC crystal plasticity models. A bold proposition is to use ML as an engine for "data-driven computational mechanics," with the goal to learn and then augment or supplant solvers for field problems, provided constraints are added to minimize error associated with the governing balance equations of physics [171]. Such approaches may be highly effective for governing equations adjoined with simple constitutive models, such as those commonly employed in linear and nonlinear elastic structural mechanics. Capuano and Rimoli [172] demonstrated that the error in solving even simple truss problems using this kind of data-driven approach may be reduced substantially by enforcing frame indifference as a constraint in ML, along with shape functions and history dependence, resulting in so-called smart finite elements. In more recent work, Logarzo *et al.* [173] demonstrated another prong to such a strategy by developing smart constitutive laws based on ML, that are trained by the kinds of information that we have often used to evaluate constitutive laws and fit parameters that can be used in lieu of traditional constitutive models to insert directly into finite elements codes as material subroutines. For history dependent continua such as metals, and for purposes of modeling behavior of microstructures/mesostructures, such an approach likely requires additional constraints associated with the physics of dislocations. Such data science strategies might excel at recognizing patterning of dislocations and considering configurations of net Burgers vector that give rise to GND strengthening, for example. A significant challenge for such approaches will lie in enforcing or framing thermodynamically consistent formulations (with proper work conjugacy of generalized forces and fluxes) and faithful input−output relations for chemo-thermomechanical coupling and multiphysics. It will be interesting to see if viable methodologies for size-dependent and microstructure-sensitive ML GC crystal plasticity will emerge in the coming decades.

In our view, potentially even more transformation may be the development of viable physics-constrained ML approaches [174] that could serve as GC crystal plasticity models, considering various model simulations and experimental information in the training process. Perhaps they will provide a superior means to objectively negotiate tradeoffs of the value of information from various models and experimental data by considering uncertainty of various sorts in ways that humans, intrinsically predisposed to certain viewpoints and biases, are less able to exercise, even with the introduction of quantitative methods to estimate model parameters. Certainly, the notion that a deep learning strategy can result in a model that is much broader than any single framework (i.e., model form generalization) is attractive. On the other hand, at this stage one can only speculate regarding the potential of smart GC crystal plasticity models. It will be interesting to consider what the role of GC models might be, either as an intermediate step towards such trends in modeling, or by serving as a skeletal generalized framework on which to constrain the training of such data-driven tools. The reader will note that we have placed particular emphasis on bottom−up models to inform mesoscale modeling, performed within the framework of GC models. Experimental information has not been heavily involved in this process, serving more as a constraint on fitting constitutive models framed at mesoscales. It is possible that smart GC models based mainly on experimental information (including very large in situ datasets) will offer purely interpolative (and necessarily limited) capabilities, while those infused with a range of bottom−up model information may have somewhat broader applicability owing to the wider range of parameter space that can be explored.

9. Conclusion

In this paper, we have provided an overview of the CAC method and its application to a wide range of coarse-grained atomistic simulations of dislocations in crystals. A reduced order GC crystal plasticity approach making use of micropolar theory inspired by Eringen's early work is outlined for 2D plane strain problems, and a possible strategy for combined use of CAC and DDD to inform model parameters is described for submicron-scale field problems.

Acknowledgments

We are grateful for the support of the collaborative NSF grant No. CMMI-1761553 (AS and DLM) with the University of Florida and ONR grant No. N00014-18-1-2784 (KC and DLM). DLM acknowledges additional support of Carter N. Paden, Jr. Distinguished Chair in Metals Processing at Georgia Tech.

Appendix A

A.1. Governing equations

The CAC method is a coarse-grained atomistics approach based on the two-level basis + lattice description of crystalline materials, i.e., a crystal is discrete at the atomic level, but continuous at the lattice level. The original Irving and Kirkwood approach [75, 76] was extended by Hardy [175] to calculate continuous local densities from discrete particles in a many-body system

$$\boldsymbol{a}(z,t) = \sum_{k=1}^{n} \boldsymbol{A}(\boldsymbol{r},\boldsymbol{p})\delta(\boldsymbol{R}^k - \boldsymbol{z}). \tag{A.1}$$

Here, the δ-function serves as the localization function that links any dynamic function in phase space $\boldsymbol{A}(\boldsymbol{r},\boldsymbol{p})$ to an equivalent local

density function in real space $\boldsymbol{a}(\boldsymbol{z},t)$. Chen [9] extended this to a system containing N_l unit cells and N_a atoms per unit cell. The ensemble-averaged local density function can then be given in physical space as

$$\bar{\boldsymbol{a}}(\boldsymbol{x},\boldsymbol{y},t)=\left\langle\sum_{k=1}^{N_l}\sum_{\xi=1}^{N_a-1}\boldsymbol{A}(\boldsymbol{r}_{k\xi},\boldsymbol{v}_{k\xi})\delta(\boldsymbol{x}-\boldsymbol{r}_k)\delta(\boldsymbol{y}-\Delta\boldsymbol{r}_{k\xi})\right\rangle, \quad (A.2)$$

where vectors $\boldsymbol{x}$, $\boldsymbol{y}$, respectively, denote the large- and small-scale location variations in physical space, vector $\boldsymbol{r}_k$ denotes the location of the unit cell, and $\Delta\boldsymbol{r}_{k\xi}$ denotes the position of atoms in that unit cell. Expressing Eq. (A.2) in terms of the per unit cell volume V of cell k located at $\boldsymbol{x}$

$$\boldsymbol{a}(\boldsymbol{x},t)=\sum_{k=1}^{N_l}\left(\sum_{\xi=1}^{N_a}\boldsymbol{A}(\boldsymbol{r}_{k\xi},\boldsymbol{v}_{k\xi})\right)\delta_V(\boldsymbol{x}-\boldsymbol{r}_k)=\sum_{\alpha=1}^{N_a}\boldsymbol{a}_\alpha(\boldsymbol{x},t). \quad (A.3)$$

The contribution of the αth atom to $\boldsymbol{a}(\boldsymbol{x},t)$ in a volume element of $V_\alpha(V=\sum_\alpha V_\alpha)$ can be further defined as

$$\begin{aligned}\boldsymbol{a}_\alpha(\boldsymbol{x},t)&=\sum_{k=1}^{N_l}\sum_{\xi=1}^{N_a}\boldsymbol{A}(\boldsymbol{r}_{k\xi},\boldsymbol{v}_{k\xi})\delta_V(\boldsymbol{x}-\boldsymbol{r}_k)\delta_{V\alpha}(\boldsymbol{y}-\Delta\boldsymbol{r}_{k\xi})\\&=\boldsymbol{a}(\boldsymbol{x},\boldsymbol{y},t).\end{aligned} \quad (A.4)$$

The delta functions serve as box functions, which are defined on the specific unit cell and are zero elsewhere; similarly, they are defined for the target atom in the unit cell and are zero elsewhere

$$\delta_V(\boldsymbol{x}-\boldsymbol{r}_k)\equiv\frac{1}{V}\begin{cases}1 & \text{if } \boldsymbol{x}-\boldsymbol{r}_k\in V,\\ 0 & \text{if } \boldsymbol{x}-\boldsymbol{r}_k\notin V,\end{cases} \quad (A.5)$$

$$\delta_{V\alpha}(\boldsymbol{y}-\Delta\boldsymbol{r}_{k\xi})\equiv\begin{cases}1 & \text{if } \boldsymbol{y}-\Delta\boldsymbol{r}_{k\xi}\in V_\alpha \quad \text{or } \xi=\alpha,\\ 0 & \text{if } \boldsymbol{y}-\Delta\boldsymbol{r}_{k\xi}\notin V \quad \text{or } \xi\neq\alpha.\end{cases} \quad (A.6)$$

Chen *et al.* [128] defines $\boldsymbol{a}(\boldsymbol{x},\boldsymbol{y},t)$ as an atomic-scale local density function. Averaging over discrete time stepping intervals Δt as in typical MD simulations, the equations for local contribution to mass density, momentum density, and energy density become

$$\rho_\alpha(\boldsymbol{x},t)=\sum_{k=1}^{N_l}\sum_{\xi=1}^{N_a}m_{k\xi}\bar{\delta}_V(\boldsymbol{x}-\boldsymbol{r}_k)\bar{\delta}_{V\alpha}(\boldsymbol{y}-\Delta\boldsymbol{r}_{k\xi}), \quad (A.7)$$

$$\rho_\alpha\boldsymbol{v}_\alpha(\boldsymbol{x},t)=\sum_{k=1}^{N_l}\sum_{\xi=1}^{N_a}m_\xi\boldsymbol{v}_{k\xi}\bar{\delta}_V(\boldsymbol{x}-\boldsymbol{r}_k)\bar{\delta}_{V\alpha}(\boldsymbol{y}-\Delta\boldsymbol{r}_{k\xi}), \quad (A.8)$$

$$\begin{aligned}E_\alpha(\boldsymbol{x},t)=&\sum_{k=1}^{N_l}\sum_{\xi=1}^{N_a}\left(\frac{1}{2}m_\xi v_{k\xi}^2+\Phi_{k\xi}\right)\bar{\delta}_V(\boldsymbol{x}-\boldsymbol{r}_k)\\&\times\bar{\delta}_{V\alpha}(\boldsymbol{y}-\Delta\boldsymbol{r}_{k\xi}).\end{aligned} \quad (A.9)$$

Here, $\bar{\delta}_V$, $\bar{\delta}_{V\alpha}$ are the averages of δ_V, $\delta_{V\alpha}$, respectively, over the time interval Δt. $\Phi_{k\xi}$ is the site potential energy which can be computed, for instance, using an empirical interatomic potential. Time evolution of conserved quantities can then be expressed in terms of a lattice-level flux $\boldsymbol{J}_1$ and atomic-scale flux $\boldsymbol{J}_2$ as

$$\begin{aligned}\frac{\partial}{\partial t}\boldsymbol{a}_\alpha(\boldsymbol{x},t)=&-\frac{1}{V}\oiint_{\partial V}\boldsymbol{J}_1(\boldsymbol{x}+\boldsymbol{x}',t)\cdot\boldsymbol{n}\,dS\\&-\frac{1}{V}\oiint_{\partial V_\alpha}\boldsymbol{J}_2(\boldsymbol{y}+\boldsymbol{y}',t)\cdot\boldsymbol{n}\,dS_\alpha.\end{aligned} \quad (A.10)$$

Here, $\boldsymbol{n}$ is the outward unit normal vector, and ∂V, ∂V_α are the unit cell and internal dividing surfaces, shown schematically in Fig. A.1. Flux $\boldsymbol{J}_2$ does not cross the surface ∂V.

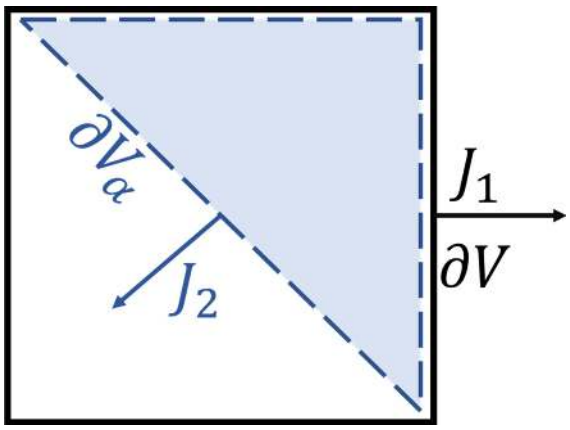

Fig. A.1. Schematic showing the division between external unit cell flux and internal unit cell flux.

The integral form of Eq. (A.8) for conservation of mass can be given as

$$\begin{aligned}\frac{\partial}{\partial t}\rho_\alpha(\boldsymbol{x},t)=&\sum_{k=1}^{N_l}\sum_{\xi=1}^{N_a}m_{k\xi}\frac{\partial}{\partial t}\bar{\delta}_V(\boldsymbol{x}-\boldsymbol{r}_k)\bar{\delta}_{V\alpha}(\boldsymbol{y}-\Delta\boldsymbol{r}_{k\xi})\\&+\sum_{k=1}^{N_l}\sum_{\xi=1}^{N_a}m_{k\xi}\bar{\delta}_V(\boldsymbol{x}-\boldsymbol{r}_k)\frac{\partial}{\partial t}\bar{\delta}_{V\alpha}(\boldsymbol{y}-\Delta\boldsymbol{r}_{k\xi})\\=&-\frac{1}{V}\oiint_{\partial V}\rho_\alpha\boldsymbol{v}\cdot\boldsymbol{n}\,dS\\&-\frac{1}{V}\oiint_{\partial V_\alpha}\rho_\alpha(\boldsymbol{v}_\alpha-\boldsymbol{v})\cdot\boldsymbol{n}\,dS_\alpha,\end{aligned} \quad (A.11)$$

where $\boldsymbol{v}=\partial\boldsymbol{x}/\partial t$ and $\boldsymbol{v}_\alpha=\boldsymbol{p}_\alpha/\rho_\alpha$. Stated more succinctly

$$\frac{\partial\rho_\alpha}{\partial t}=-\nabla_x\cdot(\rho_\alpha\boldsymbol{v})-\nabla_{y\alpha}\cdot(\rho_\alpha\Delta\boldsymbol{v}_\alpha). \quad (A.12)$$

Similarly for linear momentum

$$\begin{aligned}\frac{\partial(\rho_\alpha\boldsymbol{v}_\alpha)}{\partial t}=&\nabla_x\cdot(\boldsymbol{t}_\alpha-\rho_\alpha\boldsymbol{v}\otimes(\boldsymbol{v}+\Delta\boldsymbol{v}_\alpha))\\&+\nabla_{y\alpha}\cdot(\boldsymbol{\tau}_\alpha-\rho_\alpha\Delta\boldsymbol{v}_\alpha\otimes(\boldsymbol{v}+\Delta\boldsymbol{v}_\alpha))+\boldsymbol{f}_{\text{ext}},\end{aligned} \quad (A.13)$$

where $\boldsymbol{f}_{\text{ext}}$ is an external force field, and $\boldsymbol{t}_\alpha$ and $\boldsymbol{\tau}_\alpha$ are the momentum flux through ∂V and ∂V_α, respectively. Energy flux is then written as

$$\begin{aligned}\frac{\partial(\rho_\alpha e_\alpha)}{\partial t}=&\nabla_x\cdot(\boldsymbol{q}_\alpha+\boldsymbol{t}_\alpha(\boldsymbol{v}+\Delta\boldsymbol{v}_\alpha)-\boldsymbol{v}\rho_\alpha e_\alpha)\\&+\nabla_{y\alpha}\cdot(\boldsymbol{j}_\alpha+\boldsymbol{\tau}_\alpha\cdot(\boldsymbol{v}+\Delta\boldsymbol{v}_\alpha)-\Delta\boldsymbol{v}_\alpha\rho_\alpha e_\alpha)\\&+\boldsymbol{f}_{\text{ext}}\cdot(\boldsymbol{v}+\Delta\boldsymbol{v}_\alpha),\end{aligned} \quad (A.14)$$

where $\boldsymbol{q}_\alpha$ and $\boldsymbol{j}_\alpha$ are the heat flux vectors through ∂V and ∂V_α, respectively. By substituting the conservation equations into the linear momentum equation, we arrive at the governing equation of CAC

$$\begin{aligned}\rho_\alpha\ddot{\boldsymbol{u}}_\alpha=&\boldsymbol{f}_\alpha^{\text{int}}(\boldsymbol{x})+\boldsymbol{f}_\alpha^{\text{ext}}(\boldsymbol{x})+\frac{1}{V}\oiint_{\partial V}\boldsymbol{t}_\alpha^{\text{kin}}dS\\&+\frac{1}{V_\alpha}\oiint_{\partial V_\alpha}\boldsymbol{\tau}_\alpha^{\text{kin}}dS_\alpha,\end{aligned} \quad (A.15)$$

where $\boldsymbol{t}_\alpha^{\text{kin}}$ and $\boldsymbol{\tau}_\alpha^{\text{kin}}$ denote the kinetic stresses.

A.2. Finite element approach

The development of the CAC governing law, presented in previous section, follows Chen *et al.* [128]. The primary difference in this work results from the method of solution. The finite element implementation in this work extends the work of Xu *et al.* [18] to allow for multiple internal unit cell DOF. The finite element method can be used to solve equation (A.15), with the weak (Galerkin) form over an element,

$$\iiint_{V_e} S_\eta(\rho_\alpha \ddot{\boldsymbol{u}}_\alpha - \boldsymbol{f}_\alpha^{\text{int}} - \boldsymbol{f}_\alpha^{\text{ext}} - \boldsymbol{f}_\alpha^{T}) dV = \boldsymbol{0}. \tag{A.16}$$

Here, S_η represents the FE shape function, $\boldsymbol{f}_\alpha^{\text{int}}$ is the internal force density contribution of αth atom, $\boldsymbol{f}_\alpha^{\text{ext}}$ is the external body force field acting on the αth atom, and $\boldsymbol{f}_\alpha^{T}$ is the force associated with temperature. When using energy minimization to approximate quasi-static conditions or quenched dynamics that drive the temperature to zero in conditions without external body forces, this governing equation takes the simplified form

$$\iiint_{V_e} S_\eta(\rho_\alpha \ddot{\boldsymbol{u}}_\alpha - \boldsymbol{f}_\alpha^{\text{int}}) dV = \boldsymbol{0}. \tag{A.17}$$

Much of previous published work using CAC utilizes trilinear shape functions of the form

$$S_\eta = \frac{1}{8}(1 \pm \chi)(1 \pm \eta)(1 \pm \zeta), \tag{A.18}$$

where χ, η and ζ are natural coordinates. Within an element, the displacement vector of the αth atom at position x can be interpolated from the nodal positions

$$\hat{\boldsymbol{u}}_a(\boldsymbol{x}, \boldsymbol{t}) = S_\xi(\boldsymbol{x}) \boldsymbol{U}_{\xi\alpha}(\boldsymbol{t}), \tag{A.19}$$

where $S_\xi(\boldsymbol{x})$ denotes the value of the shape function of node ξ at position $\boldsymbol{x}$ and $\boldsymbol{U}_{\xi\alpha}(\boldsymbol{t})$ denotes the displacement of the αth atom at node ξ. Equation (A.17) can then be split into two parts. The first part can be converted to the matrix form

$$\iiint_{V_e} S_\eta(\boldsymbol{x}) \rho_\alpha S_\xi(\boldsymbol{x}) \ddot{\boldsymbol{U}}_{\xi\alpha}(\boldsymbol{t}) dV = \boldsymbol{M}\boldsymbol{R}^{\xi\alpha}. \tag{A.20}$$

Here, $\boldsymbol{R}^{\xi\alpha}$ is a $3 \times N_{\text{npe}}$ matrix representing the nodal displacements at time t, with the number of nodes per element being N_{npe}, and $\boldsymbol{M}$ is the $N_{\text{npe}} \times N_{\text{npe}}$ mass matrix

$$\boldsymbol{M} = \iiint_{V_e} S_\eta(\boldsymbol{x}) \rho_\alpha S_\xi(\boldsymbol{x}) dV \tag{A.21}$$

In the previous expression the shape function terms, $S_\eta(\boldsymbol{x})$ and $S_\xi(\boldsymbol{x})$, are $1 \times N_{\text{npe}}$ vectors. The second term in the equation can be replaced by a quadrature with the form

$$\iiint_{V_e} S_\eta(\boldsymbol{x}) \boldsymbol{f}_\alpha^{\text{int}} dV = \sum_{\mu}^{N_{\text{ipe}}} \omega'_{\mu\alpha} S_{\mu\xi} \boldsymbol{f}_{\mu\alpha}. \tag{A.22}$$

Here, $\omega'_{\mu\alpha}$ represents the quadrature weight in terms of the force density for the αth atom, N_{ipe} is the number of integration points per element, $S_{\mu\xi}$ is a $1 \times N_{\text{npe}}$ matrix containing the shape function values for each node at the quadrature point position, and $\boldsymbol{f}_{\mu\alpha}$ is a 1×3 vector representing the internal force density at the quadrature point for the αth atom. While the integration point can be any material point within the finite element, defining the quadrature points for the αth atom as actual atoms allows for a more straightforward calculation with the quadrature force being related to the atomic force via

$$\boldsymbol{f}_{\mu\alpha} = \frac{\mathbf{F}^{\mu\alpha}}{\Omega^\mu}. \tag{A.23}$$

Here, $\mathbf{F}^{\mu\alpha}$ is defined as the atomic force vector for the αth atom at the integration point unit cell and Ω^μ is the volume of the μth integration point. Combining expressions (A.20), (A.22) and (A.23) into (A.17) leads to

$$\boldsymbol{M}\boldsymbol{R}^{\xi\alpha} - \sum_{\mu}^{N_{\text{ipe}}} \omega_\mu S_{\mu\xi} \mathbf{F}^{\mu\alpha} = \boldsymbol{0} \tag{A.24}$$

with a new quadrature weight term

$$\omega_\mu = \frac{\omega'_\mu}{\Omega^\mu}. \tag{A.25}$$

Numerous choices of quadrature points, μ, and weights, ω_μ, are possible; however, it is required that the summation of weights equals the number of unit cells per element. Integration points must be carefully selected as the local force density function/can be a highly non-linear function of x. Furthermore, the local force density can have large degrees of variation within a finite element, as the element surface is more sensitive to external influence than interior atoms. This variation can be seen, for instance, in the case in which a dislocation propagates between finite element discontinuities. The variation of force/energy density fields is contained primarily within a few layers of unit cells near the surface of the finite elements. Unit cells within the finite element interior have mostly homogenous force/energy densities. Overcoming this can be done, as proposed by Xu *et al.* [18], by splitting the finite element region into subregions which are assumed to have quasi-constant local force densities except at the boundary between subregions. The governing equation of CAC then takes the form

$$\boldsymbol{M}\boldsymbol{R}^{\xi\alpha} - \sum_{\gamma}^{N_{\text{spe}}} \sum_{\mu}^{N_{\text{ips}}} \omega_\mu S_{\mu\xi} \mathbf{F}^{\mu\alpha} = \boldsymbol{0}, \tag{A.26}$$

where N_{spe} is the number of subregions per element and N_{ips} is the number of integration points in each subregion. Further notes on this splitting of finite elements into subregions are found in Ref. 18.

References

[1] A. C. Eringen. Mechanics of micromorphic continua, in *Mechanics of Generalized Continua*, ed. E. Kröner (Springer, Berlin), 1968.
[2] G. A. Maugin. Generalized continuum mechanics: what do we mean by that?, in *Mechanics of Generalized Continua. Advances in Mechanics and Mathematics*, ed. G. Maugin and A. Metrikine, Vol. 21 (Springer, New York), pp. 3–13, 2010.
[3] G. A. Maugin. Generalized continuum mechanics: Various paths, in *Continuum Mechanics Through the Twentieth Century. Solid Mechanics and Its Applications*, Vol. 196 (Springer, Dordrecht), pp. 223–241, 2013.
[4] G. A. Maugin. Some remarks on generalized continuum mechanics. *Mathematics and Mechanics of Solids* **20**(3), pp. 280–291, 2015.
[5] E. B. Tadmor, M. Ortiz and R. Phillips. Quasicontinuum analysis of defects in solids. *Philosophical Magazine A* **73**(6), pp. 1529–1563 (1996a).
[6] E. B. Tadmor, R. Phillips and M. Ortiz. Mixed atomistic and continuum models of deformation in solids. *Langmuir* **12**(19), pp. 4529–4534 (1996b).
[7] R. Miller, E. B. Tadmor, R. Phillips and M. Ortiz. Quasicontinuum simulation of fracture at the atomic scale. *Modelling and Simulation in Materials Science and Engineering* **6**(5), pp. 607–638 (1998a).
[8] R. Miller, M. Ortiz, R. Phillips, V. Shenoy and E. B. Tadmor. Quasicontinuum models of fracture and plasticity. *Engineering Fracture Mechanics* **61**(3–4), pp. 427–444 (1998b).

[9] Y. Chen. Reformulation of microscopic balance equations for multiscale materials modeling. *Journal of Chemical Physics* **130**, 134706, 2009.
[10] Y. Chen, J. Zimmerman, A. Krivtsov and D. L. McDowell. Assessment of atomistic coarse-graining methods. *International Journal of Engineering Science* **49**, pp. 1137–1349, 2011.
[11] Y. Chen, S. Shabanov and D. L. McDowell. Concurrent atomistic-continuum modeling and simulation of crystalline materials. *Journal of Applied Physics* **126**, 101101, 2019.
[12] Y. Chen, S. Shabanov and D. L. McDowell. Erratum: Concurrent atomistic-continuum modeling of crystalline materials. *Journal of Applied Physics* **130**, 019903, 2021.
[13] A. Diaz, D. L. McDowell and Y. Chen. The limitations and successes of concurrent dynamic multiscale modeling methods at the mesoscale, in *Generalized Models and Non-classical Approaches in Complex Materials 2. Advanced Structured Materials*, eds. H. Altenbach, J. Pouget, M. Rousseau, B. Collet and T. Michelitsch, Vol 90 (Springer, Cham), 2018.
[14] L. Xiong, G. J. Tucker, D. L. McDowell and Y. Chen. "Coarse-grained atomistic simulation of dislocations. *Journal of the Mechanics and Physics of Solids* **59**, pp. 160–177, 2011.
[15] L. Xiong, Q. Deng, G. J. Tucker, D. L. McDowell and Y. Chen. A concurrent scheme for passing dislocations from atomistic to continuum regions. *Acta Materialia* **60**(3), pp. 899–913 (2012a).
[16] L. Xiong, Q. Deng, G. J. Tucker, D. L. McDowell and Y. Chen. Coarse-grained atomistic simulations of dislocations in Al, Ni and Cu crystals. *International Journal of Plasticity* **38**, pp. 86–101 (2012b).
[17] L. Xiong, S. Xu, D. L. McDowell and Y. Chen. Concurrent atomistic-continuum simulations of dislocation-void interactions in FCC crystals. *International Journal of Plasticity* **65**, pp. 33–42, 2015.
[18] S. Xu, R. Che, L. Xiong, Y. Chen and D. L. McDowell. A quasistatic implementation of the concurrent atomistic-continuum method for FCC crystals. *International Journal of Plasticity* **72**, pp. 91–126, 2015.
[19] S. Xu, L. Xiong, Y. Chen and D. L. McDowell. Sequential slip transfer of mixed character dislocations across Σ3 coherent twin boundary in FCC metals: A concurrent atomistic-continuum study. *NPJ Computational Materials* **2**, 15016 (2016a).
[20] S. Xu, L. Xiong, Q. Deng and D. L. McDowell. Mesh refinement schemes for the concurrent atomistic-continuum method. *International Journal of Solids and Structures* **90**, pp. 144–152 (2016b).
[21] S. Xu, L. Xiong, Y. Chen and D. L. McDowell. An analysis of key characteristics of the frank-read source process in FCC metals. *Journal of the Mechanics and Physics of Solids* **96**, pp. 460–476 (2016c).
[22] S. Xu, J. Rigelesaiyin, L. Xiong, Y. Chen and D. L. McDowell. Generalized continua concepts in coarse-graining atomistic simulations, in *Generalized Models and Non-classical Approaches in Complex Materials 2. Advanced Structured Materials*, eds. H. Altenbach *et al.*, Vol. 90 (Springer, Cham), pp. 237–260, 2018.
[23] Y. U. Wang, Y. M. Jin, A. M. Cuitino and A. G. Khachaturyan. Nanoscale phase field microelasticity theory of dislocations: Model and 3D simulations. *Acta Materialia* **49**(10), pp. 1847–1857, 2001.
[24] C. Shen and Y. Wang. Modeling dislocation network and dislocation–precipitate interaction at mesoscopic scale using phase field method. *International Journal of Multiscale Computational Engineering* **1**(1), pp. 91–104, 2003.
[25] Y. Wang and J. Li. Phase field modeling of defects and deformation. *Acta Materialia* **58**(4), pp. 1212–1235, 2010.
[26] J. R. Mianroodi and B. Svendsen. Atomistically determined phase-field modeling of dislocation dissociation, stacking fault formation, dislocation slip, and reactions in fcc systems. *Journal of the Mechanics and Physics of Solids* **77**, pp. 109–122, 2015.
[27] J. Lepinoux and L. P. Kubin. The dynamic organization of dislocation structures: A simulation. *Scripta Metallurgica* **21**, pp. 833–838, 1987.
[28] A. N. Gulluoglu, D. J. Srolovitz, R. Lesar and P. S. Lomdahl. Dislocation distributions in two dimensions. *Scripta Metallurgica* **23**, pp. 1347–1352, 1989.
[29] R. J. Amodeo and N. M. Ghoniem. A review of experimental-observations and theoretical-models of dislocation cells and subgrains. *Res Mechanica* **23**(2–3), pp. 137–160, 1988.
[30] R. J. Amodeo and N. M. Ghoniem. Dislocation dynamics. I. A proposed methodology for micromechanics. *Physics Review B* **41**, 6958, 1990.
[31] N. M. Ghoniem. A perspective on dislocation dynamics, in *Handbook of Materials Modeling Volume 1: Methods and Models*, ed. S. Yip (Springer, Netherlands), pp. 1–7, 2005.
[32] I. Groma. Link between the microscopic and mesocopic length-scale description of the collective behavior of dislocations. *Physical Review B* **56**(10), 5807–5813, 1997.
[33] I. Groma. Statistical physical approach to describe the collective properties of dislocations, in *Multiscale Modelling of Plasticity and Fracture by Means of Dislocation Mechanics*, Vol. 522 (Springer, Vienna), 2010.
[34] A. Arsenlis and D. M. Parks. Crystallographic aspects of geometrically-necessary and statistically-stored dislocation density. *Acta Materialia* **47**(5), pp. 1597–1611 (1999).
[35] A. Arsenlis and D. M. Parks. Modeling the evolution of crystallographic dislocation density in crystal plasticity. *Journal of the Mechanics and Physics of Solids* **50**, pp. 1979–2009, 2002.
[36] A. El-Azab. Statistical mechanics treatment of the evolution of dislocation distributions in single crystals. *Physical Review B* **61**(18), pp. 11956–11966, 2000.
[37] A. El-Azab. Statistical mechanics of dislocation systems. *Scripta Materialia* **54**, pp. 723–727, 2006.
[38] M. Zaiser. Statistical modeling of dislocation system. *Material Science and Engineering A* **309–310**, pp. 304–315, 2001.
[39] R. LeSar and J. M. Rickman. Incorporation of local structure in continuous theory of dislocations. *Physical Review B* **69**, 172105, 2004.
[40] A. El-Azab, J. Deng and M. Tang. Statistical characterization of dislocation ensembles. *Philosophical Magazine* **87**(8–9), pp. 1201–1223, 2007.
[41] T. Hochrainer, M. Zaiser and P. Gumbsch. A three-dimensional continuum theory of dislocation systems: kinematics and mean-field formulation. *Philosophical Magazine* **87**, pp. 1261–1282, 2007.
[42] T. Hochrainer, S. Sandfeld, M. Zaiser and P. Gumbsch. Continuum dislocation dynamics: Towards a physical theory of crystal plasticity. *Journal of the Mechanics and Physics of Solids* **63**, pp. 167–178, 2014.
[43] J. Deng and A. El-Azab. Temporal statistics and coarse graining of dislocation ensembles. *Philosophical Magazine* **90**(27–28), pp. 3651–3678, 2010.
[44] P. D. Ispánovity, I. Groma, G. Györgyi, P. Szabó and W. Hoffelner. Criticality of relaxation in dislocation systems. *Physical Review Letters* **107**(8), 085506, 2011.
[45] S. Sandfeld, T. Hochrainer, M. Zaiser and P. Gumbsch. Continuum modeling of dislocation plasticity: Theory, numerical implementation, and validation by discrete dislocation simulations. *Journal of Materials Research* **26**(5), pp. 623–632, 2011.
[46] S. Xia and A. El-Azab. Computational modelling of mesoscale dislocation patterning and plastic deformation of single crystals. *Modelling and Simulation in Materials Science and Engineering* **23**(5), pp. 55009–55034, 2015.
[47] O. Kapetanou, D. Weygand and M. Zaiser. Stress and strain fluctuations in plastic deformation of crystals with disordered microstructure. *Journal of Statistical Mechanics: Theory and Experiment* **2015**(8), 08009, 2015.
[48] I. Groma, M. Zaiser and P. D. Ispánovity. Dislocation patterning in a two-dimensional continuum theory of dislocations. *Physical Review B* **93**(21), 214110, 2016.
[49] M. Monavari, S. Sandfeld and M. Zaiser. Continuum representation of systems of dislocation lines: A general method for deriving closed-form evolution equations. *Journal of the Mechanics and Physics of Solids* **95**, pp. 575–601, 2016.
[50] E. P. Busso, F. T. Meissonnier and N. P. O'Dowd. Gradient-dependent deformation of two-phase single crystals. *Journal of the Mechanics and Physics of Solids* **48**, pp. 2333–2361 (2000).
[51] M. E. Gurtin. A gradient theory of single-crystal viscoplasticity that accounts for geometrically necessary dislocations. *Journal of the Mechanics and Physics of Solids* **50**(1), pp. 5–32, 2002.
[52] L. P. Evers, W. A. M. Brekelmans and M. G. D. Geers. Non-local crystal plasticity model with intrinsic SSC and GND effects. *Journal of the Mechanics and Physics of Solids* **52**, pp. 2379–2401, 2004.
[53] K. S. Cheong, E. P. Busso and A. Arsenlis. A study of microstructural length scale effects on the behaviour of FCC polycrystals using strain gradient concepts. *International Journal of Plasticity* **21**(9), pp. 1797–1814, 2005.
[54] C. J. Bayley, W. A. M. Brekelmans and M. G. D. Geers. A comparison of dislocation-induced back stress formulations in strain gradient crystal plasticity. *International Journal of Solids and Structures* **43**, pp. 7268–7286, 2006.
[55] M. E. Gurtin and L. Anand. A gradient theory for single-crystal plasticity. *Modelling and Simulation in Materials Science and Engineering* **15**, pp. 263–270, 2007.
[56] G. Z. Voyiadjis and R. K. Abu Al-Rub. Gradient plasticity theory with a variable length scale parameter. *International Journal of Solids and Structures* **42**(14), pp. 3998–4029 (2005).
[57] E. M. Viatkina, W. A. M. Brekelmans and M. G. D. Geers. Modelling of the internal stress in dislocation cell structures. *European Journal of Mechanics A/Solids* **26**, pp. 982–998, 2007.

[58] J. M. Gerken and P. R. Dawson. A crystal plasticity model that incorporates stresses and strains due to slip gradients. *Journal of the Mechanics and Physics of Solids* **56**(4), 1651–1672, 2008.
[59] F. P. E. Dunne, R. Kiwanuka and A. J. Wilkinson. Crystal plasticity analysis of micro-deformation, lattice rotation and geometrically necessary dislocation density. *Proceedings of the Royal Society A* **468**, pp. 2509–2531, 2012.
[60] S. Bargmann and B. Svendsen. Theoretical and algorithmic formulation of models for energetic GND-based hardening in single crystals. *Journal for Multiscale Computational Engineering* **10**(6), pp. 551–565, 2012.
[61] O. Aslan, N. M. Cordero, A. Gaubert and S. Forest. Micromorphic approach to single crystal plasticity and damage. *International Journal of Engineering Science* **49**(12), pp. 1311–1325, 2011.
[62] N. M. Cordero, A. Gaubert, S. Forest, E. P. Busso, F. Gallerneau and S. Kruch. Size effects in generalised continuum crystal plasticity for two-phase laminates. *Journal of the Mechanics and Physics of Solids* **58**, pp. 1963–1994, 2010.
[63] N. M. Cordero, S. Forest and E. P. Busso. Micromorphic modelling of grain size effects in metal polycrystals. *GAMM-Mitteilungen* **36**(2), pp. 186–202, 2013.
[64] S. Forest, J. R. Mayeur and D. L. McDowell. Micromorphic crystal plasticity, in *Handbook of Nonlocal Continuum Mechanics for Materials and Structures*, ed. G. Voyiadjis (Springer, Cham), 2018.
[65] J. D. Clayton, D. J. Bammann, and D. L. McDowell. A geometric framework for the kinematics of crystals with defects. *Philosophical Magazine* **85** (33–35), pp. 3983–4010, 2005.
[66] J. R. Mayeur and D. L. McDowell. Bending of single crystal thin films as predicted by micropolar crystal plasticity. *International Journal of Engineering Science* **49**, pp. 1357–1366, 2011.
[67] J. R. Mayeur and D. L. McDowell. An evaluation of higher-order single crystal strength models for constrained thin films subjected to simple shear. *Journal of the Mechanics and Physics of Solids* **61**(9), pp. 1935–1954, 2013.
[68] J. R. Mayeur and D. L. McDowell. A comparison of Gurtin-type and micropolar single crystal plasticity with generalized stresses. *International Journal of Plasticity* **57**, pp. 29–51, 2014.
[69] J. R. Mayeur and D. L. McDowell. Micropolar crystal plasticity simulations of particle strengthening. *Modeling and Simulation in Materials Science and Engineering* **23**(6), 065007, 2015.
[70] J. R. Mayeur, D. L. McDowell and S. Forest. Micropolar crystal plasticity, in *Handbook of Nonlocal Continuum Mechanics for Materials and Structures*, ed. G. Voyiadjis (Springer, Cham), pp. 1–47, 2018.
[71] D. L. McDowell. Viscoplasticity of heterogeneous metallic materials. *Materials Science and Engineering R: Reports* **62**(3), pp. 67–123, 2008.
[72] D. L. McDowell. A perspective on trends in multiscale plasticity. *International Journal of Plasticity* **26**(9), pp. 1280–1309, 2010.
[73] D. L. McDowell. Multiscale modeling of interfaces, dislocations, and dislocation field plasticity, in *Mesoscale Models. CISM International Centre for Mechanical Sciences (Courses and Lectures)*, eds. S. Mesarovic, S. Forest and H. Zbib, Vol. 587 (Springer, Cham), pp. 195–297, 2019.
[74] D. L. McDowell. Microstructure-sensitive computational structure-property relations in materials design, in *Computational Materials System Design*, eds. D. Shin and J. Saal (Springer, Cham), pp. 1–25, 2018.
[75] J. G. Kirkwood. The statistical mechanical theory of transport processes. I. General theory. *Journal Chemical Physics* **14**, 180, 1946.
[76] J. Irving and J. G. Kirkwood. The statistical mechanical theory of transport processes. IV. The equations of hydrodynamics. *Journal of Chemical Physics* **18**, pp. 817–829 (1950).
[77] Y. Chen and J. Lee. Atomistic formulation of a multiscale field theory for nano/micro solids. *Philosophical Magazine* **85**(33–35), pp. 4095–4126, 2005.
[78] Y. Chen. Local stress and heat flux in atomistic systems involving three-body forces. *The Journal of Chemical Physics* **124**(5), 054113, 2006.
[79] L. Xiong, D. L. McDowell and Y. Chen. Sub-THz phonon drag on dislocations by coarse-grained atomistic simulations. *International Journal of Plasticity* **55**, pp. 268–278 (2014a).
[80] L. Xiong, X. Chen, D. L. McDowell and Y. Chen. Predicting phonon properties of 1D polyatomic crystals through the concurrent atomistic-continuum simulations. *Archives Applied Mechanics* **84**, 1665–1675 (2014b).
[81] P. A. Pluchino, X. Chen, M. Garcia, L. Xiong, D. L. McDowell and Y. Chen. Dislocation migration across coherent phase interfaces in SiGe superlattices. *Computational Materials Science* **111**, pp. 1–6, 2016.
[82] S. Silling, M. Epton, O. Weckner, J. Xu and E. Askari. Peridynamic states and constitutive modeling. *Journal of Elasticity* **88**, pp. 151–184, 2007.
[83] S. Sun and V. Sundararaghavan. A peridynamic implementation of crystal plasticity. *International Journal of Solids and Structures* **51**, pp. 3350–3360, 2014.
[84] X. Chen, W. Li, A. Diaz, Y. Li, Y. Chen and D. L. McDowell. Recent progress in the concurrent atomistic-continuum method and its application in phonon transport. *MRS Communications* **7**(4), pp. 785–797, 2017.
[85] X. Chen, A. Diaz, L. Xiong, D. L. McDowell and Y. Chen. Passing waves from atomistic to continuum. *Journal of Computational Physics* **354**, pp. 393–402, 2018.
[86] K. Chu, A. Diaz, Y. Chen, T. Zhu and D. L. McDowell. Multiscale concurrent atomistic-continuum (CAC) modeling of multicomponent alloys. *Computational Materials Science* **201**, 110873, 2022.
[87] L. M. Dupuy, E. B. Tadmor, R. E. Miller and R. Phillips. Finite-temperature quasicontinuum: Molecular dynamics without all the atoms. *Physical Review Letters* **95**, 060202 (2005).
[88] E. B. Tadmor, F. Legoll, W. K. Kim, L. M. Dupuy and R. E. Miller. Finite-temperature quasi-continuum. *Applied Mechanics Reviews* **65**(1) 010803, 2013.
[89] R. E. Rudd and J. Q. Broughton. Coarse-grained molecular dynamics and the atomic limit of finite elements. *Physical Review B* **58**(10), pp. 5893–5896, 1998.
[90] R. E. Rudd and J. Q. Broughton. Concurrent coupling of length scales in solid state systems. *Physica Status Solidi B* **217**(1), pp. 251–291, 2000.
[91] S. Xu, L. Xiong, Y. Chen and D. L. McDowell. Validation of the concurrent atomistics-continuum method on screw dislocation/stacking fault interactions. *Crystals* **7**(5) 120 (2017a).
[92] S. Xu, L. Xiong, Y. Chen and D. L. McDowell. Comparing EAM potentials to model slip transfer of sequential mixed character dislocations across two symmetric tilt grain boundaries in Ni. *JOM* **69**(5), pp. 814–821 (2017b).
[93] S. Xu, D. L. McDowell and I. Beyerlein. Sequential obstacle interactions with dislocations in a planar array. *Acta Materialia* **174**, pp. 160–172, 2019.
[94] A. Selimov, S. Xu, Y. Chen and D. L. McDowell. Lattice dislocation induced misfit dislocation evolution in semi-coherent {111} bimetal interfaces. *Journal of Materials Research* **36**, pp. 2763–2778, 2021.
[95] J. R. Rice. Inelastic constitutive relations for solids: An internal variable theory and its application to metal plasticity. *Journal of the Mechanics and Physics of Solids* **19**, pp. 433–455, 1971.
[96] W. Muschik. *Non-equilibrium Thermodynamics with Application to Solids* (Springer-Verlag, New York), 1993.
[97] G. Henkelman, B. P. Uberuaga and H. Jonsson. A climbing image nudged elastic band method for finding saddle points and minimum energy paths. *Journal of Chemical Physics* **113**(22), pp. 9901–9904, 2000.
[98] T. Zhu, J. Li and S. Yip. Atomistic reaction pathway sampling: The nudged elastic band method and nanomechanics applications, in *Nano and Cell Mechanics: Fundamentals and Frontiers*, eds. H. D. Espinosa and G. Bao (John Wiley & Sons LTD, West Sussex, United Kingdom), 2013.
[99] J. Fan. *Multiscale Analysis of Deformation and Failure of Materials*, Vol. 5 (John Wiley and Sons LTD, West Sussex, United Kingdom), 2011.
[100] S. Shao, J. Wang, A. Misra and R. G. Hoagland. Spiral patterns of dislocations at nodes in (111) semi-coherent FCC interfaces. *Scientific Reports* **3**(1), pp. 1–7, 2013.
[101] M. Xiang, Y. Liao, K. Wang, G. Lu and J. Chen. Shock-induced plasticity in semi-coherent {111} Cu-Ni multilayers. *International Journal of Plasticity* **103**, pp. 23–38 (2018).
[102] X. Tian, J. Cui, M. Yang, K. Ma and M. Xiang. Molecular dynamics simulations on shock response and spalling behaviors of semi-coherent {111} Cu-Al multilayers. *International Journal of Mechanical Sciences* **172**, 105414, 2020.
[103] Y. Chen and A. Diaz. Physical foundation and consistent formulation of atomic-level fluxes in transport processes. *Physical Review E* **98**, 052113, 2018.
[104] H. Yang, L. Zhu, R. Zhang, J. Zhou and Z. Sun. Shearing dominated by the coupling of the interfacial misfit and atomic bonding at the FCC (111) semi-coherent interfaces. *Materials & Design* **186**, 108294, 2020.
[105] R. F. Zhang, T. C. Germann, X. Y. Liu, J. Wang and I. J. Beyerlein. Layer size effect on the shock compression behavior of fcc–bcc nanolaminates. *Acta Materialia* **79**, pp. 74–83, 2014.
[106] R. J. Dikken and M. K. Salehani. Edge dislocation impingement on interfaces between dissimilar metals, ffhal-01572509f (2017), https://hal.archives-ouvertes.fr/hal-01572509/document.
[107] S. Xu, Y. Li and Y. Chen. Si/Ge (111) Semicoherent interfaces: Responses to an in-plane shear and interactions with lattice dislocations. *Physica Status Solidi (b)* **257**(12), 2000274, 2020.
[108] X. Y. Chen, X. F. Kong, A. Misra, D. Legut, B. N. Yao, T. C. Germann and R. F. Zhang. Effect of dynamic evolution of misfit dislocation pattern on dislocation nucleation and shear sliding at semi-coherent bimetal interfaces. *Acta Materialia* **143**, pp. 107–120, 2018.

[109] G. J. Tucker, J. A. Zimmerman and D. L. McDowell. Continuum metrics for deformation and microrotation from atomistic simulations: Application to grain boundaries. *International Journal of Engineering Science* **49**(12), pp. 1424–1434, 2011.

[110] J. A. Zimmerman, D. J. Bammann and H. Gao. Deformation gradients for continuum mechanical analysis of atomistic simulations. *International Journal of Solids and Structures* **46**(2), pp. 238–253, 2009.

[111] A. Stukowski and K. Albe. Dislocation detection algorithm for atomistic simulations. *Modelling and Simulation in Materials Science and Engineering* **18**(2), 025016, 2010.

[112] C. Varvenne, A. Luque, W. G. Nöhring and W. A. Curtin. Average-atom interatomic potential for random alloys. *Physical Review B* **93**, 104201, 2016.

[113] K. Chu, M. E. Foster, R. B. Sills, X. Zhou, T. Zhu and D. L. McDowell. Temperature and composition dependent screw dislocation mobility in austenitic stainless steels from large-scale molecular dynamics. *NPJ Computational Materials* **6**, 179, 2020.

[114] D. Farkas. Deformation behavior of a model high entropy alloy from atomistic simulations. *Materials Science and Engineering: A* **812**, 141124, 2021.

[115] W. R. Jian, Z. Xie, S. Xu, Y. Su, X. Yao and J. J. Beyerlein. Effects of lattice distortion and chemical short-range order on the mechanisms of deformation in medium entropy alloy CoCrNi. *Acta Materialia* **199**, pp. 352–369, 2020.

[116] E. Antillon, C. Woodward, S. I. Rao, B. Akdim and T. A. Parthasarathy. A molecular dynamics technique for determining energy landscapes as a dislocation percolates through a field of solutes. *Acta Materialia* **166**, pp. 658–676, 2019.

[117] S. Nag, T. Junge and W. A. Curtin. Atomistic-continuum coupling of random alloys. *Modelling and Simulation in Materials Science and Engineering* **27**, 075004, 2019.

[118] G. Bussi, D. Donadio and M. Parinello. Canonical sampling through velocity rescaling. *Journal of Chemical Physics* **126**, 014101, 2007.

[119] C. M. Castelluccio and D. L. McDowell. Mesoscale cyclic crystal plasticity with dislocation substructures. *International Journal of Plasticity* **98**, pp. 1–26, 2017.

[120] U. F. Kocks, A. S. Argon and M. F. Ashby. Thermodynamics and kinetics of slip, in *Progress in Materials Science*, 1st edn. (Pergamon Press, New York), 1975.

[121] A. M. Hussein, S. I. Rao, M. D. Uchic, D. M. Dimiduk and J. A. El-Awady. Microstructurally based cross-slip mechanisms and their effects on dislocation microstructure evolution in fcc crystals. *Acta Materialia* **85**, pp. 180–190, 2015.

[122] H. M. Zbib and T. Diaz de la Rubia. A multiscale model of plasticity. *International Journal of Plasticity* **18**, pp. 1133–1163, 2002.

[123] W. Ee, W. Ren and F. Vanden-Eijnden. Simplified and improved string method for computing the minimum energy paths in barrier crossing events. *Journal of Chemical Physics* **126**(16), 164103, 2007.

[124] M. D. Sangid, T. Ezaz, H. Sehitoglu and I. M. Robertson. Energy of slip transmission and nucleation at grain boundaries. *Acta Materialia* **59**, pp. 283–296, 2011.

[125] H. Jónsson, G. Mills and K. W. Jacobsen. Nudged elastic band method for finding minimum energy paths of transitions, in *Proceedings of the International School of Physics*, eds. B. J. Berne and G. Ciccotti and D. F. Coker (World Scientific), pp. 385–404, 1998, https://doi.org/10.1142/3816.

[126] S. Plimpton. Fast parallel algorithms for short-range molecular dynamics. *Journal of Computational Physics* **117**, pp. 1–19, 1995.

[127] T. Zhu, J. Li, A. Samanta, H. G. Kim and S. Suresh. Interfacial plasticity governs strain rate sensitivity and ductility in nanostructured metals. *Proceedings of the National Academy of Sciences* **104**, pp. 3031–3036, 2007.

[128] D. Chen, L. L. Costello, C. B. Geller, T. Zhu and D. L. McDowell. Atomistic modeling of dislocation cross-slip in nickel using free-end nudged elastic band method. *Acta Materialia* **168**, pp. 436–447, 2019.

[129] C. Sobie, L. Capolungo, D. L. McDowell and E. Martinez. Scale transition using dislocation dynamics and the nudged elastic band method. *Journal of the Mechanics and Physics of Solids* **105**, pp. 161–178, 2017.

[130] R. J. Asaro. Crystal plasticity. *ASME Journal of Applied Mechanics* **50**, pp. 921–934 (1983a).

[131] R. J. Asaro. Micromechanics of crystals and polycrystals. *Advances in Applied Mechanics* **23**, pp. 1–115 (1983b).

[132] C. Shen, J. Li and Y. Wang. Predicting structure and energy of dislocations and grain boundaries. *Acta Materialia* **74**, pp. 125–131, 2014.

[133] W. Cai, A. Arsenlis, C. R. Weingberger and V. V. Bulatov. A non-singular continuum theory of dislocations. *Journal of the Mechanics and Physics of Solids* **54**, pp. 561–587 (2006).

[134] A. Arsenlis, W. Cai, M. Tang, M. Rhee, T. Oppelstrup, G. Hommes, T. G. Pierce and V. V. Bulatov. Enabling strain hardening simulations with dislocation dynamics. *Modelling and Simulation in Materials Science and Engineering* **15**, pp. 553–595, 2007.

[135] M. Tang, G. Hommes, S. Aubry and A. Arsenlis. ParaDiS-FEM dislocation dynamics simulation code primer, https://www.osti.gov/servlets/purl/1037843/ (accessed 24 August 2021).

[136] B. Devincre, R. Madec, G. Monnet, S. Queyreau, R. Gatti and L. Kubin. Modeling crystal plasticity with dislocation dynamics simulations: The 'microMegas' code, in *Mechanics of Nano-Objects* (Presses de l'Ecole des Mines de Paris, Paris), pp. 81–100, 2011.

[137] A. M. Hussein and J. A. El-Awady. Quantifying dislocation microstructure evolution and cyclic hardening in fatigued face-centered cubic single crystals. *Journal of the Mechanics and Physics of Solids* **91**, pp. 126–144, 2016.

[138] A. C. Eringen and W. D. ClausJr.A micromorphic approach to dislocation theory and its relation to several existing theories, in *Fundamental Aspects of Dislocation Theory 2*, ed. J. A. Simmons, R. de Wit and R. Bullough (National Bureau of Standards, USA), pp. 1023–1040, 1970.

[139] A. C. Eringen. Nonlocal polar elastic continua. *International Journal of Engineering Science* **10**, 1–16, 1972.

[140] A. C. Eringen. *Microcontinuum Field Theories. I. Foundations and Solids*, Vol. 487 (Springer-Verlag, New York), 1999.

[141] O. W. Dillon and J. Kratochvíl. A strain gradient theory of plasticity. *International Journal of Solids and Structures* **6**, pp. 1513–1533, 1970.

[142] D. J. Bammann and E. C. Aifantis. On a proposal for a continuum with microstructure. *Acta Mechanica* **45**, pp. 91–121, 1982.

[143] D. J. Bammann and E. C. Aifantis. A model for finite-deformation plasticity. *Acta Mechanica* **69**, pp. 97–117, 1987.

[144] H. B. Muhlhaus and E. C. Aifantis. A variational principle for gradient plasticity. *International Journal of Solids and Structures* **28**, pp. 845–857, 1991.

[145] N. A. Fleck and J. W. Hutchinson. A phenomenological theory for strain gradient effects in plasticity. *Journal of the Mechanics and Physics of Solids* **41**, pp. 1825–1857 (1993).

[146] N. A. Fleck and J. W. Hutchinson. A reformulation of strain gradient plasticity. *Journal of the Mechanics and Physics of Solids* **49**, pp. 2245–2271, 2001.

[147] N. A. Fleck, G. M. Muller, M. F. Ashby and J. W. Hutchinson. Strain gradient plasticity: Theory and experiments. *Acta Metallurgica Materialia* **42**, pp. 475–487, 1994.

[148] W. D. Nix and H. Gao. Indentation size effects in crystalline materials: A law for strain gradient plasticity. *Journal of the Mechanics and Physics of Solids* **46**(3), pp. 411–425, 1998.

[149] J. R. Mayeur, D. L. McDowell and D. J. Bammann. Dislocation-based micropolar single crystal plasticity: Comparison of multi- and single-criterion theories. *Journal of Mechanics and Physics of Solids* **59**(2), pp. 398–422, 2011.

[150] W. Claus and A. Eringen. Three dislocation concepts and micromorphic mechanics, in Developments in Mechanics, Proceedings of the 12th Midwestern Mechanics Conference, Vol. 6, pp. 349–358, 1969.

[151] S. Forest, F. Barbe and G. Cailletaud. Cosserat modelling of size effects in the mechanical behaviour of polycrystals and multi-phase materials. *International Journal of Solids and Structures* **37**, pp. 7105–7126, 2000.

[152] S. Forest and R. Sievert. Elastoviscoplastic constitutive frameworks for generalized continua. *Acta Mechanica* **160**, pp. 71–111, 2003.

[153] M. Rys, S. Forest and H. Petryk. A micromorphic plasticity model with the gradient-enhanced incremental hardening law. *International Journal of Plasticity* **128**, 102655, 2020.

[154] S. Forest, G. Cailletaud and R. W. Sievert. A Cosserat theory for elastoviscoplastic single crystals at finite deformation. *Archives of Mechanics* **49**, pp. 705–736, 1997.

[155] R. E. Miller and A. Acharya. A stress-gradient based criterion for dislocation nucleation in crystals. *Journal of the Mechanics and Physics of Solids* **42**(7), pp. 1507–1525 (2004).

[156] S. S. Chakravarthy and W. A. Curtin. Stress-gradient plasticity. *Proceedings of the National Academy of Science USA* **108**, pp. 15716–15720, 2011.

[157] S. Olarnrithinun, S. S. Chakravarthy and W. A. Curtin. Discrete dislocation modeling of fracture in plastically anisotropic metals. *Journal of the Mechanics and Physics of Solids* **61**, pp. 1391–1406, 2013.

[158] N. Taheri-Nassaj and H. M. Zbib. On dislocation pile-ups and stress-gradient dependent plastic flow. *International Journal of Plasticity* **74**, pp. 1–16, 2015.

[159] H. Lyu, N. Taheri-Nassaj and H. M. Zbib. A multiscale gradient-dependent plasticity model for size effects. *Philosophical Magazine* **96**(18), pp. 1883–1908, 2016.

[160] H. Mecking and U. F. Kocks. Kinetics of flow and strain-hardening. *Acta Metallurgica* **29**, pp. 1865–1875, 1981.

[161] J. F. Nye. Some geometrical relations in dislocated crystals. *Acta Metallurgica* **1**, pp. 153–162, 1953.

[162] E. Kröner. Initial studies of a plasticity theory based upon statistical mechanics, in *Inelastic Behaviour of Solids*, eds. M. Kanninen, W. Adler, A. Rosenfield and R. Jaffee (McGraw-Hill, New York), pp. 137–147, 1969.
[163] N. B. Burbery, G. Po, R. Das, N. Ghoniem and W. G. Ferguson. Dislocation dynamics in polycrystals with atomistic-informed mechanisms of dislocation — grain boundary interactions. *Journal of Micromechanics and Molecular Physics* **2**(1), 1750003, 2017.
[164] J. Y. Shu, N. A. Fleck, E. van der Giessen and A. Needleman. Boundary layers in constrained plastic flow: Comparison of nonlocal and discrete dislocation plasticity. *Journal of the Mechanics and Physics of Solids* **49**, pp. 1361–1395, 2001.
[165] S. Yefimov, I. Groma and E. van der Giessen. A comparison of a statistical-mechanics based plasticity model with discrete dislocation plasticity calculations. *Journal of the Mechanics and Physics of Solids* **52**, pp. 279–300, 2004.
[166] D. J. Luscher, D. L. McDowell and C. A. Bronkhorst. Essential features of fine scale boundary conditions for second gradient multiscale homogenization of statistical volume elements. *Journal for Multiscale Computational Engineering* **10**(5), pp. 461–486, 2012.
[167] A. Tallman, L. P. Swiler, Y. Wang and D. L. McDowell. Reconciled top-down and bottom-up hierarchical multiscale calibration of bcc Fe crystal plasticity. *International Journal for Computer Methods in Engineering* **15**(6), pp. 1–19, 2017.
[168] A. E. Tallman, K. S. Stopka, L. P. Swiler, Y. Wang, S. R. Kalidindi and D. L. McDowell. Gaussian process-driven adaptive sampling for reduced order modeling of texture effects in polycrystalline alpha-Ti. *JOM* **71**, pp. 2646–2656 (2019a).
[169] A. E. Tallman, L. P. Swiler, Y. Wang and D. L. McDowell. Hierarchical multiscale model calibration and validation for materials applications, in *Uncertainty in Multiscale Materials Modeling*, eds. Y. Wang and D. L. McDowell (Elsevier Ltd., Kidlington Oxford, United Kingdom), pp. 449–471, 2020.
[170] A. E. Tallman, L. P. Swiler, Y. Wang and D. L. McDowell. Hierarchical top-down bottom-up calibration with consideration for uncertainty and inter-scale discrepancy of peierls stress of bcc Fe. *Modeling and Simulation in Materials Science and Engineering* **27**(6) 064004 (2019b).
[171] T. Kirchdoerfer and M. Ortiz. Data-driven computational mechanics. *Computer Methods in Applied Mechanics and Engineering* **304**, pp. 81–101, 2015.
[172] G. Capuano and J. J. Rimoli. Smart finite elements: A novel machine learning application. *Computer Methods in Applied Mechanics and Engineering* **345**, pp. 363–381, 2019.
[173] H. J. Logarzo, G. Capuano and J. J. Rimoli. Smart constitutive laws: Inelastic homogenization through machine learning. *Computer Methods in Applied Mechanics and Engineering* **373**, 113482, 2021.
[174] Y. Zhu, N. Zabaras, P.-S. Koutsourelakis and P. Perdikaris. Physics-constrained deep learning for high-dimensional surrogate modeling and uncertainty quantification without labeled data. *Journal of Computational Physics* **394**(1), pp. 56–81, 2019.
[175] R. J. Hardy. Formulas for determining local properties in molecular-dynamics simulations: Shock waves. *Journal of Chemical Physics* **76**(1), pp. 622–628, 1982.